UV and U-band luminosity functions from CLAUDS and HSC-SSP – I. Using four million galaxies to simultaneously constrain the very faint and bright regimes to z ∼ 3

Thibaud Moutard, Marcin Sawicki, Stéphane Arnouts, Anneya Golob, Jean Coupon, Olivier Ilbert, Xiaohu Yang, Stephen Gwyn

Monthly Notices
of the
ROYAL ASTRONOMICAL SOCIETY

MNRAS **494,** 1894–1918 (2020)
Advance Access publication 2020 March 16

doi:10.1093/mnras/staa706

UV and *U*-band luminosity functions from CLAUDS and HSC-SSP – I. Using four million galaxies to simultaneously constrain the very faint and bright regimes to $z \sim 3$

Thibaud Moutard [1]★ Marcin Sawicki [1,2]† Stéphane Arnouts,[3] Anneya Golob,[1] Jean Coupon,[4] Olivier Ilbert,[3] Xiaohu Yang[5] and Stephen Gwyn[2]

[1]*Department of Astronomy and Physics and Institute for Computational Astrophysics, Saint Mary's University, 923 Robie Street, Halifax, NS, B3H 3C3, Canada*
[2]*NRC Herzberg Astronomy and Astrophysics, 5071 West Saanich Road, Victoria BC V9E 2E7, Canada*
[3]*Aix Marseille Université, CNRS, LAM – Laboratoire d'Astrophysique de Marseille, 38 rue F. Joliot-Curie, F-13388 Marseille, France*
[4]*Astronomical Observatory of the University of Geneva, ch. d'Ecogia 16, 1290 Versoix, Switzerland*
[5]*Department of Astronomy, Shanghai Jiao Tong University, Dongchuan RD 800, 200240 Shanghai, China*

Accepted 2020 February 19. Received 2020 February 19; in original form 2019 November 1

ABSTRACT

We constrain the rest-frame FUV (1546 Å), NUV (2345 Å), and *U*-band (3690 Å) luminosity functions (LFs) and luminosity densities (LDs) with unprecedented precision from $z \sim 0.2$ to $z \sim 3$ (FUV, NUV) and $z \sim 2$ (*U* band). Our sample of over 4.3 million galaxies, selected from the CFHT Large Area *U*-band Deep Survey (CLAUDS) and HyperSuprime-Cam Subaru Strategic Program (HSC-SSP) data lets us probe the very faint regime (down to $M_{\rm FUV}$, $M_{\rm NUV}$, $M_U \simeq -15$ at low redshift), while simultaneously detecting very rare galaxies at the bright end down to comoving densities $<10^{-5}$ Mpc^{-3}. Our FUV and NUV LFs are well fitted by single-Schechter functions, with faint-end slopes that are very stable up to $z \sim 2$. We confirm, but self-consistently and with much better precision than previous studies, that the LDs at all three wavelengths increase rapidly with lookback time to $z \sim 1$, and then much more slowly at $1 < z <$ 2–3. Evolution of the FUV and NUV LFs and LDs at $z < 1$ is driven almost entirely by the fading of the characteristic magnitude, $M^\star_{\rm UV}$, while at $z > 1$ it is due to the evolution of both $M^\star_{\rm UV}$ and the characteristic number density $\phi^\star_{\rm UV}$. In contrast, the *U*-band LF has an excess of faint galaxies and is fitted with a double-Schechter form; $M^\star_U$, both $\phi^\star_U$ components, and the bright-end slope evolve throughout $0.2 < z < 2$, while the faint-end slope is constant over at least the measurable $0.05 < z < 0.6$. We present tables of our Schechter parameters and LD measurements that can be used for testing theoretical galaxy evolution models and forecasting future observations.

Key words: galaxies: evolution – galaxies: luminosity function, mass function – galaxies: star formation – galaxies: statistics – ultraviolet: galaxies.

1 INTRODUCTION

The galaxy luminosity function (LF) and its redshift evolution is one of the most fundamental ways to characterize the galaxy population. It provides a direct probe of the hierarchical framework of galaxy formation. Defined by $\phi(L)\,{\rm d}L$ as the comoving number density of galaxies with luminosity between L and $L + {\rm d}L$, the LF is a wavelength-dependent measurement that gives a direct test on the modelling of the baryonic physics such as star formation activity, dust attenuation, and feedback processes. This paper is concerned with galaxy LFs at rest-frame ultra-violet (UV: $\lambda = 1000$–3000 Å) and *u* ($\lambda = 3000$–4000 Å) wavelengths. In this wavelength regime, light in star-forming galaxies is thought to be primarily produced by short-lived massive stars. For this reason, the evolution of the UV LF has historically been used as a probe of the evolution of star-forming activity in the galaxy population.

Similarly, the UV luminosity density (LD) ($\rho_{\rm UV}$) – which is the luminosity-weighted integral of the LF, $\int L \times \phi(L)\,{\rm d}L$ – is a direct measurement of the unobscured cosmic star formation density (SFRD, $\rho_{\rm SFR}$) and its evolution with redshift, giving us a sketch of the cosmic star formation history. At $0 \lesssim z \lesssim 1$, this was first done by Lilly et al. (1996), with UV LF measurements from

★ E-mail: thibaud.moutard@lilo.org
† Canada Research Chair.

spectroscopic samples with optically selected sources (Lilly et al. 1995). At higher redshift, a lower limit on $\rho_{\rm SFR}$ based on Lyman-break galaxies (LBGs) was determined by Madau et al. (1996) who summed up the UV light from *U*- and *B*-band dropouts detected in the Hubble Deep Field (HDF; Williams et al. 1996), while Sawicki, Lin & Yee (1997) presented the first measurement of $\rho_{\rm SFR}$ between $z = 1$ and $z \sim 3.5$ by making use of photometric redshifts. The realization that significant fractions of UV photons are prevented from escaping from high-z star-forming galaxies by interstellar dust (e.g. Meurer et al. 1997; Sawicki & Yee 1998) forced dust corrections to be subsequently applied to this $\rho_{\rm UV} \rightarrow \rho_{\rm SFR}$ conversion method.

Subsequently, the *GALEX* satellite (Martin et al. 2005) allowed first measurements of the unobscured UV LF at $z \sim 0$ (Wyder et al. 2005; Budavári et al. 2005) and out to $z \sim 1.2$ (Arnouts et al. 2005). The later provided the first UV LF measurements over the entire redshift range $0 \leq z \leq 3.5$ by combining spectroscopically selected *GALEX* sources and photometric redshifts of optically selected sources at high redshift in the HDFs. Schiminovich et al. (2005) used those UV–LFs to estimate the evolution of the UV LD ($\rho_{\rm UV}$) and of the cosmic star formation rate density ($\rho_{\rm SFR}$) after accounting for typical UV attenuation due to interstellar dust in star-forming galaxies.

SFRD measurements made at infra-red or sub-millimetre wavelengths – which measure the stellar energy re-radiated by interstellar dust and thus obviate the needs for dust corrections – can provide a complementary picture to that gleaned from the UV. Although such measurements have been possible for some time for high-z galaxies (e.g. Hughes et al. 1998; Chapman et al. 2005; Magnelli et al. 2013; Gruppioni et al. 2013; Goto et al. 2019), they do not yet provide significant insights at very high redshifts ($z \gtrsim 6$), nor for low-mass galaxies that have low SFRs and low dust content (e.g. Bouwens et al. 2009, 2012; Sawicki 2012).

Consequently, UV LF measurements allow us the only self-consistent way to study the evolution of the galaxy population and of the SFRD *at a constant rest-frame wavelength* across the entire redshift range over which galaxies are currently known to exist, $z = 0 \sim 10$. Similarly, UV measurements let us reach galaxies that are too faint to be observed by infra-red and sub-mm surveys. This explains why UV LFs have continuously been used for estimating the evolution of the cosmic star formation rate density over the last two decades (e.g. Steidel et al. 1999; Ouchi et al. 2004; Sawicki & Thompson 2006b; Dahlen et al. 2007; Iwata et al. 2007; Reddy & Steidel 2009a; van der Burg, Hildebrandt & Erben 2010; Cucciati et al. 2012; Sawicki 2012; McLure et al. 2013b; Madau & Dickinson 2014; Bouwens et al. 2015a; Bouwens et al. 2016; Ono et al. 2018; Khusanova et al. 2020; and many others).

The advent of multiwavelength data sets that contain flux measurements at a great many wavelengths (sometime as many as several dozen – e.g. Laigle et al. 2016) allow the estimation of physical quantities for each galaxy, such as its stellar mass, and the construction of related global descriptors, such as the galaxy stellar mass functions (SMFs) and stellar mass densities (SMDs, $\rho_{M_\star}$) – e.g. Ilbert et al. (2013), Muzzin et al. (2013), Moutard et al. (2016b), and Davidzon et al. (2017). Such 'physical' measurements are an extremely powerful tool to help us understand galaxy evolution, but they suffer from some important limitations: they rely heavily on the assumptions that underpin stellar population synthesis models (e.g. Bruzual & Charlot 2003; Maraston 2005), and the spectral energy distribution (SED) – fitting technique that's used for physical parameter estimation (e.g. Sawicki & Yee 1998; Papovich, Dickinson & Ferguson 2001; see Conroy 2013 for a review). Consequently, the fidelity of the physical parameter estimates continues to be challenged by studies that show that biases may exist in commonly used approaches: for example, different galaxy star formation histories (e.g. Leja et al. 2019), the assumed stellar initial mass function (IMF; e.g. Salpeter 1955; Chabrier 2003), the common assumption that dust acts as a uniform foreground screen (see e.g. Mitchell et al. 2013), or the treatment of individual galaxies as consisting of spatially homogeneous stellar populations (e.g. Sorba & Sawicki 2015, 2018), can influence the inferred stellar masses and – consequently – SMFs and SMDs. While such 'physical' measurements are a powerful tool to help us understand galaxy evolution, model-independent measurements, such as LFs, are therefore an essential complement.

One example of direct applications of the LFs is to calibrate or validate galaxy formation models (e.g. Kitzbichler & White 2007; Lacey et al. 2011; Somerville et al. 2012; Henriques et al. 2013; Lacey et al. 2016; Sharma et al. 2016), since in using the directly measured quantity (i.e. the LF), the modeller has full control over the comparison process, rather than relying on assumptions made by the observational papers. A related use of UV LFs is in the forecasting of future observations (e.g. Williams et al. 2018; Maseda et al. 2019). Finally, because UV LFs probe the galaxy population at wavelengths close to those which ionize hydrogen, UV LFs are used in work that aims to assess the contribution of different types of objects to reionizing the Universe, or to maintaining it in its ionized state (e.g. Inoue, Iwata & Deharveng 2006; Sawicki & Thompson 2006b; Bouwens et al. 2015b; Ishigaki et al. 2018; Iwata et al. 2019).

For these reasons, it is important that we have the best possible measurements of the UV LFs over a wide redshift range of cosmic history. Although the situation has improved dramatically from the early days of the HDF, even the largest studies to date are still based on relatively small fields, such as the COSMOS field (Scoville et al. 2007), and are thus susceptible to cosmic variance and poor statistics, particularly at the bright end. With new data that we now have in hand, we can do better. In this paper, we therefore set out to provide a state-of-the-art measurement of the rest-frame FUV (1546 Å), NUV (2345 Å), and *U*-band (3690 Å) LFs using two overlapping and complementary cutting-edge surveys: the recently completed Canada–France–Hawaii Telescope (CFHT) Large Area *U*-band Deep Survey (CLAUDS; Sawicki et al. 2019) and the ongoing HyperSuprime-Cam Subaru Strategic Program (HSC-SSP; Aihara et al. 2018b). Together, these two surveys probe the Universe to an unprecedented combination of area and depth, as described in Section 2.1 and allow us to produce the most statistically significant measurements of the UV LFs that are also essentially free of cosmic variance.

This paper focuses on providing reference measurements of the rest-frame FUV, NUV, and *U*-band LFs based on these state-of-the-art surveys, notably to serve as a basis for making observational forecasts and validating theoretical models. We postpone more physically motivated interpretations to future work (see companion paper; Moutard et al. in preparation).

Throughout this paper, we use the standard cosmology ($\Omega_{\rm m} = 0.3, \Omega_\Lambda = 0.7$ with $H_0 = 70\,{\rm km\,s^{-1}\,Mpc^{-1}}$). Magnitudes are given in the AB system (Oke 1974).

2 GALAXY SAMPLE

2.1 Data

This study uses the $U + grizy$ data from the CFHT Large Area *U*-band Deep Survey (CLAUDS) and the HyperSuprime-Cam Subary

Strategic Program (HSC-SSP). These surveys are described in detail in Sawicki et al. (2019, CLAUDS) and in Aihara et al. (2018b, and references therein; HSC-SSP), and the procedures for merging the data sets are described in Sawicki et al. (2019). Consequently, here we give only a summary of the key details.

The CLAUDS and HSC-SSP imaging data overlap over four well-studied fields, namely E-COSMOS, ELAIS-N1, DEEP2-3, and XMM-LSS, each spanning ∼4–6 deg^2. The *U*-band data cover 18.60 deg^2 to a depth of $U_{\rm AB} = 27.1$ (5σ in 2 arcsec apertures), with selected ultra-deep sub-areas within the E-COSMOS and XMM-LSS fields that cover 1.36 deg^2 to a depth of $U = 27.7$ (5σ in 2 arcsec apertures). CLAUDS *U*-band data were obtained in two somewhat different CFHT/MegaCam filters: data in the ELAIS-N2 and DEEP2-3 fields were taken with the new *u* filter, while those in XMM-LSS were taken with the older u^* filter. The E-COSMOS field contains data in the *u* filter except in the central region where both *u* and u^* data overlap. The *u* and u^* data are kept separate, even in areas where they overlap. The image quality of the CLAUDS data is excellent, with median seeing of 0.92 arcsec. For the details of CLAUDS data, see Sawicki et al. (2019).

The HSC-SSP project (Aihara et al. 2018b) provides deep Subary/HSC imaging in the *grizy* wavebands in the same fields imaged by CLAUDS. Here, we use images from the S16A internal HSC-SSP data release that are deeper than the HSC-SSP public data release 1 (PDR1; Aihara et al. 2018a) with depths of $g_{\rm AB} \sim 26.6$, $r_{\rm AB} \sim 26.1$, $i_{\rm AB} \sim 25.7$, $z_{\rm AB} \sim 25.1$, and $y_{\rm AB} \sim 24.2$ (5σ in 2 arcsec apertures), though not as deep as those from the very recent PDR2 (Aihara et al. 2019). Seeing in the HSC-SSP varies from band to band, with the *i*-band providing the sharpest images (∼0.62 arcsec); in all bands, the seeing in the HSC images is even better than the (excellent) seeing in the CLAUDS *U*-band data.

Fig. 1 shows the overlap of the CLAUDS (black) and HSC–SSP (green) footprints. The footprints of the deep HSC observations are somewhat larger than those of the CLAUDS data, so the area of overlap is dictated by the extent of the CLAUDS data, i.e. 18.29 deg^2 after the masking of areas around bright stars. Our survey contains two layers of different depths:

(i) The Deep layer covers a total area of 18.29 deg^2 with $U \geq 26.8$, $g \geq 26.5$, $r \geq 26.1$, $i \geq 25.7$, $z \geq 25.1$, and $y \geq 24.2$, respectively;
(ii) While the ultra-deep layer covers an area of 1.54 deg^2 with $U \geq 27.5$, $g \geq 27.1$, $r \geq 26.9$, $i \geq 26.6$, $z \geq 26.3$, and $y \geq 25.0$, respectively.

We use the SExtractor-based multiband catalogue described in Sawicki et al. (2019). For object detection, this uses the signal-to-noise image, ΣSNR constructed from all the available uu^*grizy images as

$$\Sigma\mathrm{SNR} = \sum_{i=1}^{N} \left(\frac{f_i - \mu_i}{\sigma_i} \right), \quad (1)$$

where f_i is the flux in each pixel, σ_i is the rms width of the background sky distribution, and μ_i is its mean. Here, the index *i* runs over MegaCam bands *u* or u^* (or both, where available – i.e. in the central area of E-COSMOS) as well as the HSC bands *grizy*. Once the SExtractor software (Bertin & Arnouts 1996) has detected objects in the ΣSNR image, the multiband catalogue is then created by running SExtractor in dual image mode, with various measurements recorded for each object, including positions, fluxes (in Kron, isophotal, and fixed-radius circular apertures), fiducial radii, ellipticities, position angles, and central surface brightnesses. For more details, see Sawicki et al. (2019) and Golob et al. (in preparation). Note that the CLAUDS *U*-band images are as deep or deeper than the HSC-SSP S16A images, we used and consequently our catalogue is not expected to be biased against *U*-faint objects.

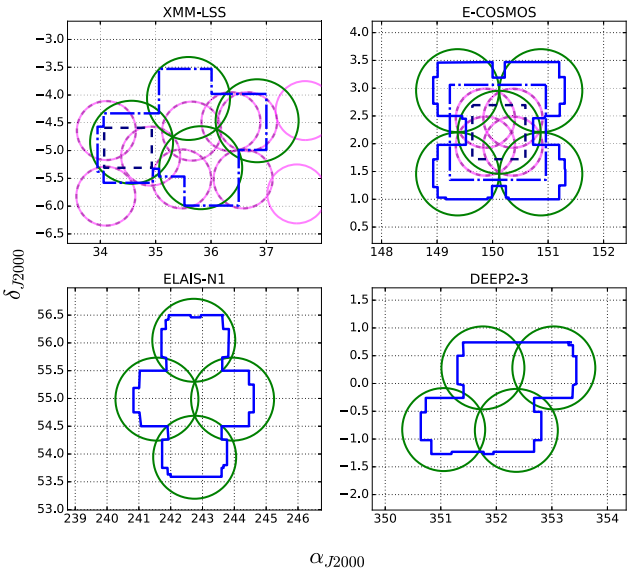

Figure 1. Footprints of the CLAUDS Deep layer *u*- and u^*-bands (blue solid and long-dash–dotted outlines, respectively) and HSC-SSP *grizy* data (green circles). The area where the two surveys overlap totals 18.60 deg^2 and reaches a median depth of $U = 27.1$, and a minimum depth of $U \geq 26.8$ (5σ in 2 arcsec apertures). The CLAUDS Ultra-Deep layer (dark-blue dashed outlines) covers 1.55 deg^2 over the XMM–LSS and E-COSMOS fields down to a minimum depth of $U \geq 27.5$. *GALEX FUV* (dark magenta dashed circles) and *NUV* (light magenta solid circles) observations overlap over 6 and 7 deg^2, respectively, down to a median depth of *FUV*, *NUV* ∼ 25.

Small apertures are known to provide less noisy colours and therefore an improved photometric redshift accuracy than total Kron-like (Kron 1980) apertures (Sawicki et al. 1997; Hildebrandt et al. 2012; Moutard et al. 2016a, b). At the same time, total fluxes are needed for deriving galaxy physical properties. Following the approach of Moutard et al. (2016a), the final magnitudes $m_{\rm FINAL}$ of each source are produced by rescaling isophotal magnitudes $m_{\rm ISO}$ to the Kron-like magnitudes $m_{\rm AUTO}$. To preserve the colours based on isophotal apertures, a mean rescaling factor δm is applied in each filter *f*:

$$m_{{\rm FINAL},f} = m_{{\rm ISO},f} + \delta m \quad (2)$$

with δm defined as

$$\delta m = \frac{\sum_f (m_{{\rm AUTO},f} - m_{{\rm ISO},f}) \times w_f}{\sum_f w_f} \quad (3)$$

for $f = u, u^*, g, r, i, z, y$, and where the weights w_f are simply defined from $\sigma_{\rm ISO}$ and $\sigma_{\rm AUTO}$, the photometric uncertainties on $m_{\rm ISO}$ and $m_{\rm AUTO}$, with $w_f = 1/\left(\sigma^2_{{\rm AUTO},f} + \sigma^2_{{\rm ISO},f}\right)$.

To properly constrain the FUV and NUV luminosities at low redshift, we complemented our photometric data set with FUV (135–175 nm) and NUV (170–275 nm) observations from the *GALEX* satellite (Martin et al. 2005). Both in the XMM-LSS and E-COSMOS fields, the *GALEX* observations we used were reduced with the EMphot code (Guillaume et al. 2006; Conseil et al. 2011) dedicated to extract UV photometry by using the CFHTLS (T0007) u^*-band detections as a priors down to $u^* \sim 25$.

Consequently, the astrometry of the resulting *GALEX* photometry is that of the CFHTLS, which enabled a straightforward position matching with our photometric data set (with 0.5 arcsec tolerance).

2.2 Galaxy identification and photometric redshift estimation

To identify and remove foreground Galactic stars, we use the machine-learning method and results of Golob et al. (in preparation). This method uses both photometric and morphological information to classify objects as stars or galaxies. In more detail, we use *HST* morphological object classification in the COSMOS field from Leauthaud et al. (2007) to train a gradient boosted tree (GBT) machine classifier to classify objects based on their CLAUDS+HSC−SSP *Ugrizy* magnitudes, colours, central surface brightnesses, and effective radii. Because the method uses photometric information, it does well even for faint objects where morphologies from ground-based imaging are ambiguous. Having trained the GBT machine classifier, we use it to remove from our sample all objects for which the classifier returned a value greater than 0.89. Doing so, we discarded ∼7.4 per cent of the sources as stars. See Golob et al. (in preparation) for details of the method and its application to our CLAUDS+HSC−SSP data set.

Our photometric redshifts are computed using a hybrid approach that combines a nearest neighbour machine-learning method (hereafter kNN; Golob in preparation; see also Sawicki et al. 2019) with the template-fitting code Le Phare (Arnouts et al. 2002; Ilbert et al. 2006).

The kNN method uses the 30-band COSMOS photometric redshifts from Laigle et al. (2016) as a training set. For each object in our catalogue, it identifies 50 nearest neighbours in colour space and then fits a weighted Gaussian kernel density estimator (KDE), with each neighbour's redshift weighted by $(d_{\rm NN} \times \Delta z)^{-1}$; here, $d_{\rm NN}$ is the Euclidean distance in colour space to the object under consideration and Δz is the width of the 68 per cent confidence interval of the neighbour's redshift in the Laigle et al. (2016) catalogue. We find that this method gives very good results on average (low scatter, σ_z, and bias, b_z) but suffers from more outliers than we would wish.

Following Moutard et al. (2016a), Le Phare photometric redshifts were computed by making use of the template library of Coupon et al. (2015), while considering four extinction laws with a reddening excess $E(B-V) \leq 0.3$, as described in Ilbert et al. (2009). In addition, as described in Ilbert et al. (2006), Le Phare tracked down and corrected for any systematic difference between the photometry and the predicted magnitudes in each band, while using the known $N(z)$ at given apparent magnitude as a prior to avoid catastrophic failures. Le Phare is thereby naturally well suited to take care of any fluctuation of the absolute calibration from field to field and to deal with the confusion between spectrum breaks in the absence of near-infrared observations.

Our hybrid photometric redshift method combines the outputs from the kNN method and Le Phare as follows. We flag outliers in the kNN photo-z catalogue and then replace their photometric redshift values with those from the Le Phare template-fitting code. Outliers are identified and flagged by comparison of the kNN redshift, $z_{\rm KDE}$, with the Le Phare redshift, $z_{\rm LPh}$. Specifically, when the threshold of $\Delta z_{\rm phot} = |z_{\rm KDE} - z_{\rm LPh}|/\sqrt{2} = 0.15 \times (1+\overline{z})$ is exceeded, with $\overline{z} = (z_{\rm KDE} + z_{\rm LPh})/2$, we adopt $z_{\rm LPh}$; otherwise we use $z_{\rm KDE}$. Doing so, we notably reduced by half the number of photo-z outliers that are due to the confusion between the Lyman and Balmer breaks.

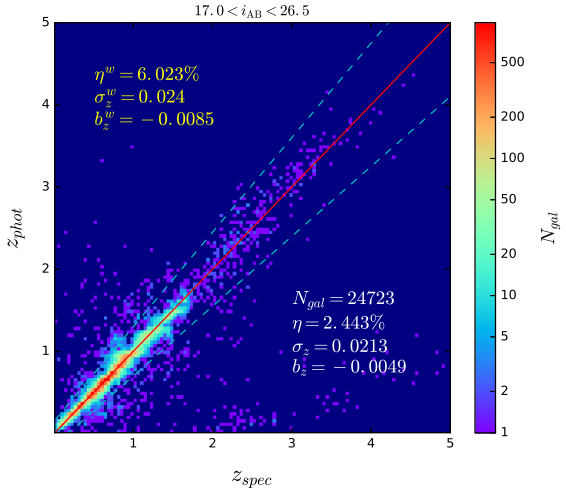

Figure 2. Comparison of our photometric redshifts with spectroscopic redshifts from Bradshaw et al. (2013); Comparat et al. (2015); Le Fèvre et al. (2013); Kriek et al. (2015); Lilly et al. (2007); Masters et al. (2017, 2019); McLure et al. (2013a); Scodeggio et al. (2018); Silverman et al. (2015); and Tasca et al. (2017). The red diagonal line shows equality (perfect match) and the dashed blue lines define outliers. The total number of galaxy spectroscopic redshifts and the usual photo-z accuracy estimators (outlier rate η, scatter σ_z and bias b_z) are reported in the lower right corner, while corresponding i-band weighted estimators are reported in the upper-left corner or the figure.

Fig. 2 shows the comparison of our hybrid photometric redshifts with a large sample of spectroscopic redshifts compiled from the literature. Overall, the hybrid photo-z quality is found to be very good within the ranges of redshift and magnitude we explore in our analysis, namely, up to $z = 3.5$ and for observed magnitudes $17.0 < i_{\rm AB} < 26.5$, with a scatter[1] of $\sigma_z = 0.0213$, a median bias[2] of $b_z = -0.0049$, and an outlier rate[3] of $\eta = 2.443$ per cent. While the spectroscopic sample we assembled combines many surveys, which makes it as representative as possible, it is much brighter (and bluer) than our photometric sample. In order to account for this effect, we followed the approach of Moutard et al. (2016b) and weighted the photo-z accuracy estimators with respect to the i-band distribution of the photometric sample. Using this approach, we found weighted scatter of $\sigma_z^w = 0.024$, weighted median bias of $b_z^w = -0.0085$ and weighted outlier rate of $\eta^w = 6.023$ per cent at $17.0 < i_{\rm AB} < 26.5$. These measurements confirmed the reliability of our hybrid photometric redshifts, which we use for the rest of the analysis that follows.

2.3 Galaxy physical parameters

2.3.1 Physical parameters and absolute magnitudes

Our procedure for estimating galaxy rest-frame FUV, NUV, and U-band magnitudes interpolates (or, in some cases – extrapolates) from the observed photometry using spectral models fitted to the photometry. We therefore describe these models (which also yield some physical parameters for our galaxies, such as their stellar

[1]Using the NMAD (normalized median absolute deviation) to define the scatter, $\sigma_z = 1.48 \times {\rm median}(\frac{|z_{\rm phot} - z_{\rm spec}|}{1+z_{\rm spec}})$.

[2]We simply define the photo-z bias as $b_z = \frac{z_{\rm phot} - z_{\rm spec}}{1+z_{\rm spec}}$.

[3]η is defined as the percentage of galaxies with $\frac{|z_{\rm phot} - z_{\rm spec}|}{1+z_{\rm spec}} > 0.15$.

masses) before moving on to describe the estimation of rest-frame magnitudes.

Absolute magnitudes and other physical parameters (stellar mass, star formation rate, etc.) were derived with the template-fitting code LE PHARE, after fixing the redshift to its best estimate (i.e. our hybrid photometric redshifts – see Section 2.2). Following Moutard et al. (2016b), we made use of the stellar population synthesis models of Bruzual & Charlot (2003) and considered two metallicities, exponentially declining star formation histories that follow $\tau^{-1}e^{-t/\tau}$ (as described in Ilbert et al. 2013), and three extinction laws with a maximum dust reddening of $E(B-V)=0.5$. Finally, we imposed a low extinction for low-SFR galaxies and the emission-line contribution was taken into account (for more details, see Moutard et al. 2016b).

We computed FUV, NUV, and *U*-band absolute magnitudes by adopting the procedure followed by Ilbert et al. (2005) to minimize the dependence of the absolute magnitudes to the template library. Specifically, to minimize the *k*-correction term, the absolute magnitude in a given passband centred on λ^0 was derived from the observed magnitude in the filter passband that was the closest from $\lambda^0 \times (1+z)$, except – to avoid measurements that are too noisy – when the apparent magnitude had an error above 0.3 mag. Moreover, all rest-frame magnitudes were derived with two different template libraries (Bruzual & Charlot 2003; Coupon et al. 2015), which allowed us to verify that no significant systematic uncertainties were introduced by the choice of template library.

2.3.2 *Absolute magnitude error budget*

Of particular importance for our analysis are the uncertainties affecting the absolute magnitudes for which we measure the LF. The first source of uncertainty is the fitting error, $\sigma_{\rm fit}$, which comes from the propagation of the photon noise. The fitting error contribution is directly estimated from the 1σ dispersion of absolute magnitudes derived from observed photometry perturbed with associated errors. The second source of uncertainty on the magnitude, $\sigma_{M,z}$, comes from the photometric redshift uncertainty. One way to estimate its effect is to compare the absolute magnitudes derived with photometric and spectroscopic redshifts. While limited by the completeness of the spectroscopic sample, it is the most comprehensive estimate of the photo-z error contribution we have access to. The last source of uncertainty we considered, $\sigma_{\rm SED}$, comes from the choice of template library used to derive absolute magnitudes. The $\sigma_{\rm SED}$ uncertainties are expected to be negligible when the *k*-correction is small, which we ensured by limiting our analysis to a redshift range where the rest-frame emission is observed in one of our filters. To estimate $\sigma_{\rm SED}$, we compared the absolute magnitudes derived from the empirical SED library (Coupon et al. 2015), $M^{\rm EMP}$, and from the stellar population synthesis models library (Bruzual & Charlot 2003), $M^{\rm SPS}$, and take $\sigma_{\rm SED} = |M^{\rm EMP} - M^{\rm SPS}|/\sqrt{2}$. The total absolute magnitude error is then given by

$$\sigma_M = \sqrt{\sigma_{\rm fit}^2 + \sigma_{M,z}^2 + \sigma_{\rm SED}^2}. \quad (4)$$

3 RESULTS

3.1 FUV, NUV, and *U*-band LFs

3.1.1 *Completeness limits and wedding cake approach*

Following an approach similar to that in Pozzetti et al. (2010), we based our estimate of the luminosity (or absolute magnitude) completeness limit on the distribution of the faintest luminosity (or absolute magnitude) at which a galaxy could have been detected at its redshift, $L_{\rm faint}$ (or $M_{\rm faint}$). In practice, if the sample is limited by the observed magnitude, m, down to the limiting depth $m \leq m_{\rm lim}$, then

$$\log(L_{\rm faint}) = \log(L) + 0.4\,(m - m_{\rm lim}) \quad (5)$$

which, in terms of absolute magnitude, gives us

$$M_{\rm faint} = M - (m - m_{\rm lim}). \quad (6)$$

In each redshift bin, we conservatively considered the 20 per cent highest redshift galaxies (i.e. those that are closest to the upper limit of the redshift bin). The corresponding absolute magnitude completeness limit, $M_{\rm lim}$, was then defined by the absolute magnitude for which 90 per cent of that upper limit population had an absolute magnitude $M < M_{\rm faint}$.

Given that our detection images combine all the CLAUDS and HSC-SSP passbands (i.e. u, u^*, g, r, i, z, y), every band contributes to the completeness limit. Assuming that a source is detected as long as it is bright enough in at least one of the bands, we derived the effective absolute magnitude completeness limit of our sample, $M_{\rm lim}$, as the faintest absolute magnitude completeness limit computed in all the bands, i.e.

$$M_{\rm lim} = \max_b \left(M_{\rm lim}^b\right), \ \text{for } b = u, u^*, g, r, i, z, y, \quad (7)$$

where $M_{\rm lim}^b$ is the absolute magnitude completeness limit derived from the limiting depth of the passband b, following equation (6).

As detailed in Section 2.1, our survey contains two layers of different depths: deep and ultra-deep. The advantage of such structure was twofold. (1) The different depths of the deep and ultra-deep layers allowed us to fine-tune our method of measuring the completeness limit by cross-matching the results from the two layers; with this, we ensure that we did not miss more than 10 per cent of galaxies in the faintest magnitude bin. (2) In order to take the best advantage of our survey, we adopted a wedding cake approach where the bright end of the LF comes from the deep layer, down to the corresponding completeness limit, below which the very faint end relies on the ultra-deep layer.

3.1.2 *LF measurement*

Given the depth of the two layers of our survey, we decided to adopt highly conservative absolute magnitude completeness limits, as discussed in the previous section, which allowed us to measure the FUV, NUV, and *U*-band LFs without incompleteness correction at $M < M_{\rm lim}$.

However, aiming to validate our method, we also measured the LFs with the tool ALF (Ilbert et al. 2005), using two different LF estimators: the $V_{\rm max}$ (Schmidt 1968) and the step-wise maximum likelihood (SWML; Efstathiou, Ellis & Peterson 1988). We verified that these two estimators were in good agreement with our uncorrected estimation of the LF down to our adopted completeness limit, which de facto confirmed our estimation of the completeness limit ($V_{\rm max}$ and SWML estimators are known to diverge below the completeness limit; Ilbert et al. 2005; Moutard et al. 2016b).

By definition, the LF, $\phi(L)\mathrm{d}L$, is defined as the comoving number density of galaxies with luminosity between L and $L+\mathrm{d}L$, or in term of absolute magnitude M, $\phi(M)\mathrm{d}M = \phi(L)\mathrm{d}(-L)$. To compute the FUV, NUV, and *U*-band LFs, we first selected a sample of 4380 629 galaxies with $z < 3.5$ in the deep layer, which covers an effective

Table 1. Demographics of our survey. Numbers in brackets indicate objects that were not used in constructing the LFs. Objects in the Overlap column were present in both the deep and ultra-deep layers and were counted only once in building the LFs.

Redshift bin	Number of galaxies Deep[a]	Ultra-deep[b]	Overlap[c]	Total used[d]
$0.05 < z < 0.3$	201 617	(*18 073*)	–	201 617
$0.3 < z < 0.45$	296 940	(*30 598*)	–	296 940
$0.45 < z < 0.6$	331 144	(*31 291*)	–	331 144
$0.6 < z < 0.9$	735 345	84 059	63 473	755 931
$0.9 < z < 1.3$	1 142 045	143 771	93 381	1192 435
$1.3 < z < 1.8$	830 481	134 570	68 037	897 014
$1.8 < z < 2.5$	566 007	102 226	58 784	609 449
$2.5 < z < 3.5$	(*277 050*)	54 977	–	54 977
$0.05 < z < 3.5$	(*277 050*)	(*79 962*)		
	4103 579	519 603	283 675	4339 507

[a]Number of galaxies in the deep layer (cf. equation 8 and Fig. 1).
[b]Number of galaxies in the ultra-deep layer (cf. equation 9 and Fig. 1).
[c]Number of galaxies present in both the deep and ultra-deep layers.
[d]Total number of galaxies considered in this study: (d) = (a) + (b) − (c).

area (i.e. after masking) of 17.02 deg^2 down to

$$(U \leq 26.9) \cup (g \leq 26.3) \cup (r \leq 25.9)$$
$$\cup (i \leq 25.5) \cup (z \leq 24.9) \cup (y \leq 24.0) \quad (8)$$

and 599 565 galaxies with $z < 3.5$ in the ultra-deep layer, which covers an effective area of 1.45 deg^2 down to

$$(U \leq 27.4) \cup (g \leq 26.9) \cup (r \leq 26.7)$$
$$\cup (i \leq 26.4) \cup (z \leq 25.9) \cup (y \leq 24.8). \quad (9)$$

As discussed in Section 2.3, we restricted our analysis to the redshift ranges $0.05 \leq z \leq 3.5$ in UV and $0.05 \leq z \leq 2.5$ in U band, where both photometric redshifts and absolute magnitudes are well constrained. We defined eight contiguous redshift bins that were chosen by considering the observed bands used to derive the absolute magnitudes: $0.05 < z \leq 0.3$, $0.3 < z \leq 0.45$, $0.45 < z \leq 0.6$, $0.6 < z \leq 0.9$, $0.9 < z \leq 1.3$, $1.3 < z \leq 1.8$, $1.8 < z \leq 2.5$, and $2.5 < z \leq 3.5$.

Table 1 summarizes the corresponding numbers of galaxies available in the two layers of our survey, as well as the numbers of galaxies we finally considered to measure the LFs after combining the two layers. Note that we only used the Deep layer to measure the LFs at $0.05 < z \leq 0.6$, given the cosmic variance affecting the ultra-deep layer at low redshift due to the limited volume it probes. On the other hand, concerning the last redshift bins we considered for the UV and U-band LFs (namely, $2.5 < z \leq 3.5$ and $1.8 < z \leq 2.5$, respectively), we only used the ultra-deep layer, given the limited depth of our g, r, i, z, y data in the deep layer. In total, we thereby made use of 4339 507 galaxies to measure the FUV, NUV, and U-band LFs.

Fig. 3 shows the FUV LF, we measured in the eight redshift bins we defined from $z = 0.05$ to $z = 3.5$. For each redshift bin, we specified the observed passband in which the FUV absolute magnitude was generally derived. At lower redshifts, our CLAUDS + HSC-SSP measurements involve an extrapolation bluewards of the observed U band, and we verify that this extrapolation is reasonable using *GALEX* data as follows. In the four lowest redshift bins, we compare the LF measured from observed *GALEX* FUV and NUV (which minimizes the k-correction) with the LF measured from CLAUDS U-band observations. As one can see, the two LF measurements are in very good agreement down to $M_{\rm FUV} \simeq -17$, -18, -18, and -19 at $0.05 < z \leq 0.3$, $0.3 < z \leq 0.45$, $0.45 < z \leq 0.6$, $0.6 < z \leq 0.9$, respectively, where we reach the depth of the *GALEX* observations.[4] This agreement suggests that the FUV absolute magnitude we derived from extrapolation of U-band observations is reliable. Similarly, Fig. 4 shows the NUV LF in the same redshift bins. In the lowest redshift bin, we compare the LF measured from *GALEX* NUV and from CLAUDS U band, and one can see that both LF measurements are in very good agreement down to $M_{\rm NUV} \simeq -17$, the depth of the *GALEX* observations. As with the FUV measurements, this agreement suggests that the NUV absolute magnitude we derived from the extrapolation of U-band observations is well constrained. Finally, in Fig. 5, we show the U-band LF we measured in the seven redshift bins from $z = 0.05$ to $z = 2.5$

In Figs 3–5, we showed the LFs we measured in the deep (squares) and ultra-deep (circles) layers. We adopted the wedding cake approach presented in the previous section when the comoving volume of the redshift bin was large enough to be characterized by an average density close to that of the Universe at that redshift (i.e. when the faint end of the LF is not dominated by the so-called cosmic variance that we discuss in the next section). One can see how at $z > 0.6$, the faint end of the LF is based on the ultra-deep layer down to the associated completeness limit, while the rest of the LF is derived from the deep layer. On the other hand, our LF measurements in the last redshift bins we considered for the UV ($2.5 < z \leq 3.5$) and U band ($1.8 < \leq 2.5$) were entirely based on the ultra-deep layer, given the very small contribution of the deep layer at those redshifts (because of its fairly bright g, r, i, z, y limits).

3.1.3 *LF uncertainties*

In addition to the Poissonian error ($\sigma_{\rm Poi}$) usually taken into account, LF measurements suffers from two additional main sources of uncertainty: the error on the luminosity or absolute magnitude (σ_M), as described in Section 2.3.2, and the so-called cosmic variance

[4]Note that *GALEX* fluxes measured with EMphot only use u band priors down to $u^* \sim 25$ (see Section 2.1).

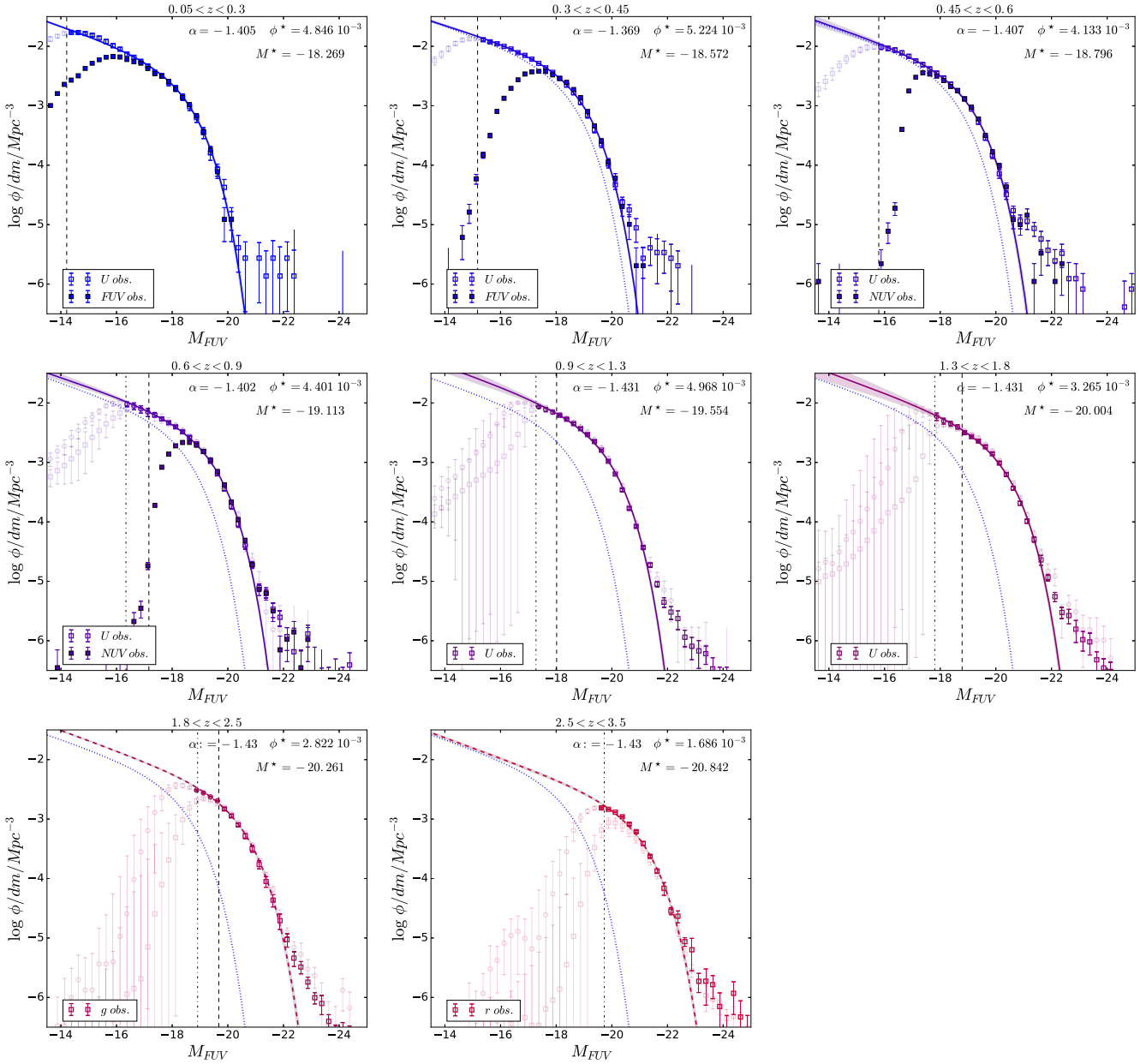

Figure 3. FUV LF measured at redshift $0.05 < z \leq 0.3$, $0.3 < z \leq 0.45$, $0.45 < z \leq 0.6$, $0.6 < z \leq 0.9$, $0.9 < z \leq 1.3$, $1.3 < z \leq 1.8$, $1.8 < z \leq 2.5$, and $2.5 < z \leq 3.5$. At $z < 0.9$, the LF based on rest-frame FUV extrapolated from our U-band data is compared with the LF derived from direct observation of the FUV luminosity in the *GALEX* FUV and NUV passbands (filed squares). At $0.6 < z < 2.5$, the faint end of the LF comes from our ultra-deep layer (open circles). At $2.5 < z < 3.5$, the whole LF is based on the ultra-deep layer. In each panel, the (solid and dashed) curve and associated envelop show our best Schechter fit and corresponding 1σ uncertainty. At $1.8 < z < 3.5$, the slope was set to $\alpha = -1.43$ (see the text) and the best Schechter fits are plotted with dashed curves. Vertical dashed and dash–dotted lines show, respectively, the location of the deep and ultra-deep layer completeness limits (see Table 2).

(σ_{cv}), which is due to large-scale inhomogeneities in the spatial distribution of galaxies in the Universe.

These additional sources of uncertainty can have an important contribution to the total error budget and therefore need to be accounted for. For instance, cosmic variance has been shown to represent a fractional error of $\sigma_{cv} = 10$–15 per cent for massive ($M_* \geq 10^{11} M_\odot$) galaxies with number densities of $\phi < 10^{-3}$ Mpc^{-3} in a 2-deg^2 survey, against $\sigma_{cv} \sim 6$–8 per cent in a 20-deg^2 survey. At the same time, the cosmic variance contribution to the error budget is small compared to the Poissonian error for very massive, i.e. rare galaxies, while it dominates the error budget for lower mass, i.e. more abundant galaxies (see Moutard et al. 2016b, for a discussion of these issues). We may expect a similar effect on the LF, where the very bright end suffers from large cosmic variance and suffers from an even larger Poissonian error, while at fainter magnitudes a modest cosmic variance dominates a very small Poissonian error.

Aiming to estimate the contribution of the cosmic variance affecting our LF measurements, we adopt the procedure followed by Moutard et al. (2016b), which is based on a method introduced by Coupon et al. (2015). In brief, at given area a, we derived cosmic variance from Jackknife resampling of N patches with area

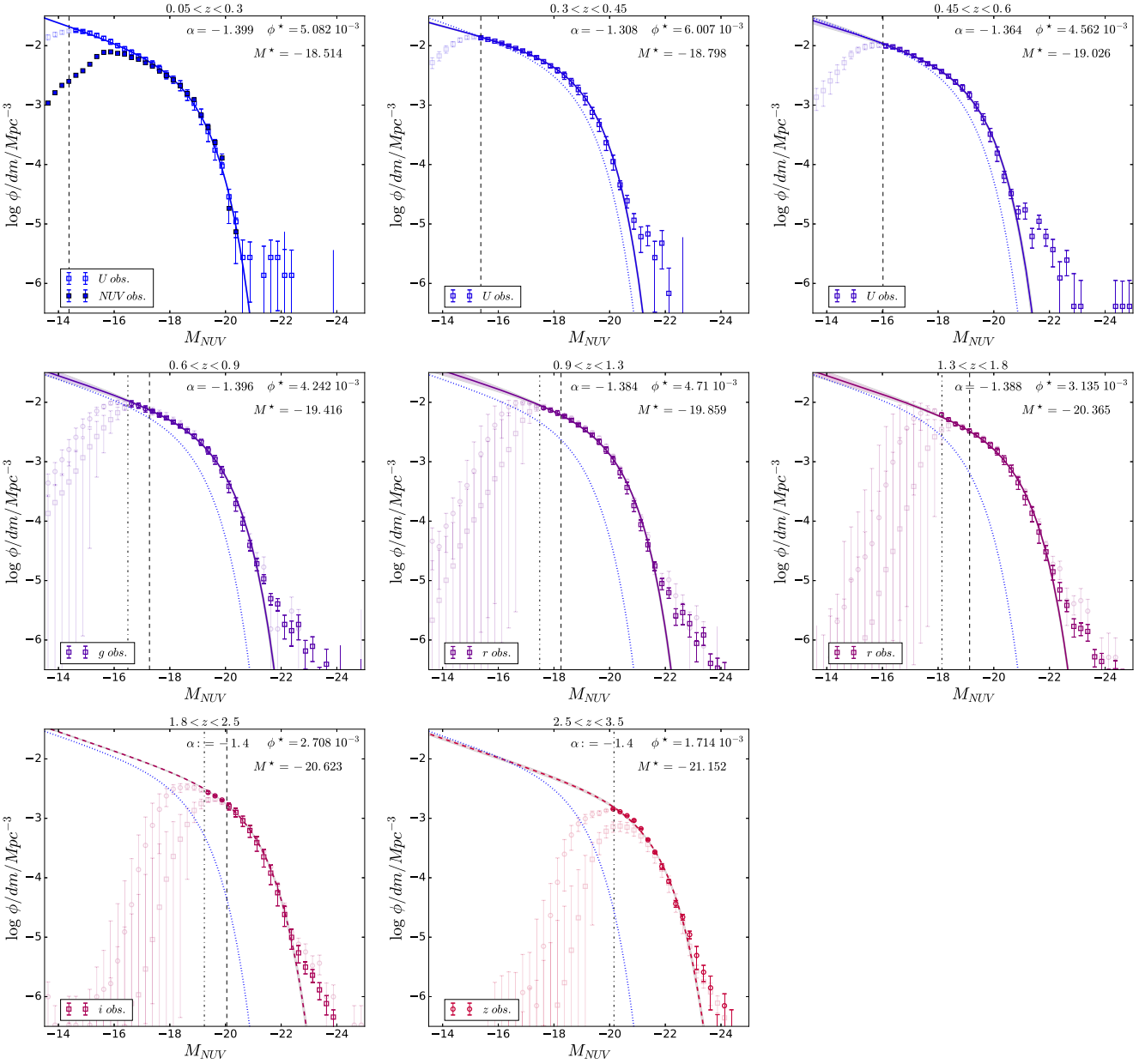

Figure 4. NUV LF measured at redshift $0.05 < z \leq 0.3$, $0.3 < z \leq 0.45$, $0.45 < z \leq 0.6$, $0.6 < z \leq 0.9$, $0.9 < z \leq 1.3$, $1.3 < z \leq 1.8$, $1.8 < z \leq 2.5$, and $2.5 < z \leq 3.5$. At $z < 0.3$, the LF based on rest-frame NUV extrapolated from our U-band data is compared with the LF derived from direct observation of the NUV luminosity in the *GALEX* NUV passband (filed squares). Similarly to Fig. 3, at $0.6 < z < 2.5$, the faint end of the LF comes from our ultra-deep layer (open circles), and at $2.5 < z < 3.5$, the whole LF is based on the ultra-deep layer. In each panel, the (solid and dashed) curve and associated envelop show our best Schechter fit and corresponding 1σ uncertainty. At $1.8 < z < 3.5$, the slope was set to $\alpha = -1.4$ (see the text) and the best Schechter fits are plotted with dashed curves. Vertical dashed and dash–dotted lines show, respectively, the location of the deep and ultra-deep layer completeness limits (see Table 2).

a, for patch areas ranging from $a = 0.2$ to 1.6 deg^2. The cosmic variance measured using subareas of our survey is then extrapolated to the total area, namely, $a = 18.29$ deg^2 and $a = 1.54$ deg^2, in the deep and ultra-deep layers, respectively (for more details on the method, please refer to Coupon et al. 2015; Moutard et al. 2016b).

The last source of uncertainty that we need to consider comes from the error on the absolute magnitude, $\sigma_{\rm M}$, as defined in Section 2.3.2. To convert $\sigma_{\rm M}$ into an error on the number density, $\sigma_{\phi,M}$, we generated 200 mock catalogues with absolute magnitudes perturbed according to σ_M (cf. equation 4) and measured the 1σ dispersion of the perturbed LFs.

The total uncertainty, σ_ϕ, affecting the LF at each magnitude bin is then calculated by combining the three sources of error in quadrature,

$$\sigma_\phi = \sqrt{\sigma^2_{\rm Poi} + \sigma^2_{\rm cv} + \sigma^2_{\phi,M}}, \quad (10)$$

and plotted in Figs 3–5.

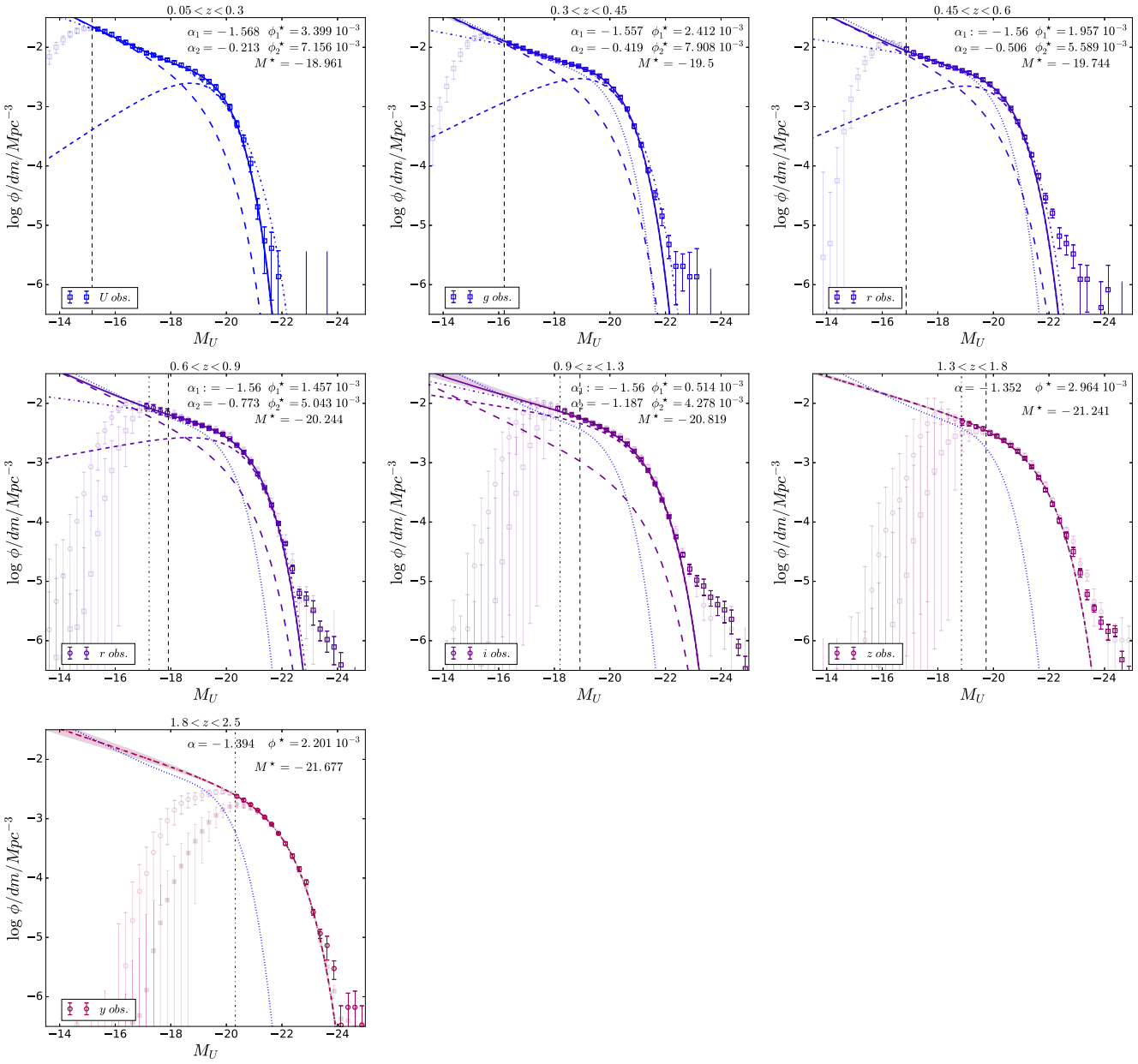

Figure 5. U-band LF measured at redshift $0.05 < z \leq 0.3$, $0.3 < z \leq 0.45$, $0.45 < z \leq 0.6$, $0.6 < z \leq 0.9$, $0.9 < z \leq 1.3$, $1.3 < z \leq 1.8$, and $1.8 < z \leq 2.5$. Similarly to Figs 3 and 4, at $0.6 < z < 1.8$, the faint end of the LF comes from our ultra-deep layer (open circles), and at $1.8 < z < 2.5$, the whole LF is based on the ultra-deep layer. In each panel, the solid line and associated envelop show our best Schechter fit and corresponding 1σ uncertainty. At $z < 1.3$, both single-Schechter (dash–dotted lines) and double-Schechter (solid lines and associated envelops) functions are shown (the two components of the double-Schechter function are shown with dashed lines). At $0.45 < z < 1.3$, the faint-end slope of the double-Schechter function was set to $\alpha_1 = -1.56$. At $1.3 < z < 2.5$, only a single Schechter was considered (see the text). Vertical dashed and dash–dotted lines show, respectively, the location of the deep and ultra-deep layer completeness limits (see Table 2).

Note that although $\sigma_{\phi,M}$ is a good estimation of the contribution of the absolute magnitude error in the LF error budget, it cannot take into account the so-called Eddington bias, whose effects we treat as discussed in Section 3.2.1.

3.2 Redshift evolution of the LFs

3.2.1 Fitting method and Eddington bias treatment

Eddington bias (Eddington 1913) affects the observed slope of the bright end of the LF by converting the statistical error on the luminosities of the more abundant (usually fainter) galaxies into a systematic boost of the number of less abundant (usually brighter) galaxies. The result of this effect is that the observed slope of the LF is shallower than the underlying reality. The same effect affects the observed SMFs, where the dominant effect is that of the scattering of lower mass galaxies into the higher mass population.

Several authors have addressed the Eddington bias over the past few years, especially regarding the high-mass end of the SMF. These studies have implicated the effect as biasing the rather mild evolution of the high-mass end of the SMF at $z < 1$ (e.g. Matsuoka &

Kawara 2010; Ilbert et al. 2013; Moutard et al. 2016b); at $z > 4$, where the SMF evolution is stronger, stellar mass uncertainties are very large and so still have to be taken into account (e.g. Caputi et al. 2011; Grazian et al. 2015; Davidzon et al. 2017). Although less discussed in the literature, the LF bright end measurements suffer from a similar effect that needs to be accounted for.

In this study, we accounted for the effects of Eddington bias by following a procedure similar to that described in Ilbert et al. (2013), as we fitted our LF measurement through χ^2 minimization. In this, we only consider the statistical uncertainties (Poisson and cosmic variance) in the χ^2 calculation during the fitting process, while the absolute magnitude uncertainty σ_M is taken into account through convolution with the fitted Schechter parametric form(s), which is thereby corrected for the Eddington bias. Adapting the approach of Moutard et al. (2016b), we consider an estimate of σ_M that varies with absolute magnitude and redshift, $\sigma_M(M, z)$, in order to avoid overcorrection of the Eddington bias.

Finally, one may notice from Figs 3–5 that the extremely bright ends of our LF measurements, typically for comoving densities $<10^{-5}$ Mpc^{-3}, suffer from uncertainties that are significantly larger than what one could expect from purely Poissonian errors. As discussed in Appendixes B and C, this is most probably due to the contamination by stars and QSOs, the identification and cleaning of which depends on the depth of our observations that varies across the survey. A very small number of interlopers is indeed sufficient to affect the actual number of extremely bright and rare galaxies. In any event, we verified that this contamination of the extremely-bright ends had not a significant impact on the fitting of the LFs that is discussed in the following.[5]

3.2.2 *FUV, NUV, and U-band LF fitting*

As can be seen in Figs 3 and 4, the Schechter parametric form (Schechter 1976) appears to be well suited to the fitting of the FUV and NUV LFs down to the completeness limits of our survey and, at least, between $z = 0.05$ and $z = 3.5$.

We therefore fitted the FUV and NUV LFs with the classical Schechter function defined as

$$\phi(L)\,\mathrm{d}L = e^{-\frac{L}{L^\star}}\,\phi^\star\left(\frac{L}{L^\star}\right)^\alpha \frac{\mathrm{d}L}{L^\star}, \tag{11}$$

which, in term of absolute magnitude, can be written as

$$\phi(M)\,\mathrm{d}M = \frac{\ln 10}{2.5}\,\phi^\star\left(10^{0.4\Delta M}\right)^{\alpha+1}\exp\left(-10^{0.4\Delta M}\right)\,\mathrm{d}M, \tag{12}$$

with $\Delta M = M^\star - M$.

While all three Schechter parameters are well constrained at $0.05 < z \leq 1.8$, the slope α and normalization $\phi^\star$ start being poorly constrained at $1.8 < z \leq 2.5$ and are no longer constrained at $z > 2.5$. One of the strengths of our data set is its ability to probe the bright end of the LF, thanks to the large area covered, the location of which is well traced by the characteristic absolute magnitude $M^\star$. Given the stability of α at $0.05 < z \leq 1.8$, we can help constraint $M^\star$ at $z > 1.8$ by setting α at $z > 1.8$ to its average value at $z \leq 1.8$: $\alpha_{z>1.8} = \mathrm{const.} = \overline{\alpha}_{z<1.8}$. Our Schechter functional fits are plotted in Figs 3 and 4 with solid lines at $z < 1.8$ and dashed lines at $z > 1.8$, and the values of the Schechter parameters are listed in Table 2.

[5]In practice, we found that the difference between the best-fitting parameters obtained by considering or excluding the LF points with comoving densities $<10^{-5}$ Mpc^{-3} was smaller than the typical error on those parameters.

While the FUV and NUV LFs are well described by the Schechter function (equation 12), this is not the case for the *U*-band LF (Fig. 5). Here, the LF shape deviates from the classical Schechter form at the faint end, where a clear upturn can be seen around $M_U \sim -17$, at least at low redshift (where our completeness limit is the faintest). Where needed, we therefore adopt a double Schechter to fit the *U*-band LF, as defined by

$$\phi(L)\,\mathrm{d}L = \mathrm{e}^{-\frac{L}{L^\star}}\left[\phi_1^\star\left(\frac{L}{L^\star}\right)^{\alpha_1} + \phi_2^\star\left(\frac{L}{L^\star}\right)^{\alpha_2}\right]\frac{\mathrm{d}L}{L^\star}, \tag{13}$$

or, in term of absolute magnitude,

$$\phi(M)\,\mathrm{d}M = \frac{\ln 10}{2.5}\left[\phi_1^\star\left(10^{0.4\Delta M}\right)^{\alpha_1+1} + \phi_2^\star\left(10^{0.4\Delta M}\right)^{\alpha_2+1}\right] \times \exp\left(-10^{0.4\Delta M}\right)\,\mathrm{d}M \tag{14}$$

with $\Delta M = M^\star - M$ and, in our case, $\alpha_1 < \alpha_2$. For further detail about the relevance of fitting, the *U*-band LF with a double-Schechter function, please refer to Appendix A.

While all the double-Schechter parameters were well constrained at $z \leq 0.5$ and could be fitted simultaneously, we had to constrain the parameters of the faint end before fitting the LF at higher redshift (notably due to the difference between the uncertainties affecting the deep and ultra-deep LF contributions, which tend to drastically reduce the ultra-deep layer contribution at the faint end of the LF in the χ^2 fitting). To constrain the fitting at $z > 0.5$, we set the faint-end slope α_1 to the its average value at $z \leq 0.45$: $\alpha_1(z > 0.45) = \mathrm{const.} = \overline{\alpha_1}_{z<0.45}$. On the other hand, at $1.3 < z \leq 2.5$, the completeness limit prevented us from observing a second Schechter component at the faint end of the LF. At these high redshifts, we only fitted the LF with a single-Schechter function. Finally, we also showed the parametric form we would obtain by fitting the *U*-band LF with a single Schechter (dash–dotted lines in Fig. 5) for comparison.

3.2.3 *Redshift evolution of the FUV, NUV, and U-band LFs*

Fig. 6 shows the redshift evolution of the fitted LF in UV and in the *U* band at $0.05 < z \leq 3.5$ and $0.05 < z \leq 2.5$, respectively. The first noteworthy feature is the evolution of the bright end of the LF, which fades continuously with cosmic time (i.e. with decreasing redshift). The second remarkable thing is the stability of the faint-end slopes in the FUV and NUV, which is clear up to $z \sim 1$. In other words, the populations of FUV and NUV bright galaxies have been continuously decreasing since $z \sim 1$, while the populations of faint galaxies in these bands have remained stable. The same trends apply to the *U*-band LF evolution, although the faint end is noisier. Additionally, it is interesting that the location of the upturn in the faint-end slope of the *U*-band LF is preserved with cosmic time, in spite of the simultaneous recession of the bright end.

We can take this analysis further by considering how the values of the Schechter parameters change with redshift. Fig. 7 shows the redshift evolution of α and $\phi^\star$ as a function of $M^\star$, corresponding to the fitted LFs shown in Fig. 6. The values of the slope α confirm the stability of the faint end seen in Fig. 6 for the FUV and NUV LFs, with $-1.42 \leq \alpha \leq -1.31$ and $-1.53 \leq \alpha \leq -1.28$ at $0.05 < z \leq 1.3$, respectively. The normalization follows a similar trend with $\phi^\star = 4.4$–6.0×10^{-3} Mpc^{-3} and $\phi^\star = 4.9$–6.6×10^{-3} Mpc^{-3} at $0.05 < z \leq 1.3$ for the FUV and NUV LFs, respectively. The characteristic absolute magnitude is characterized by a clear fading of $\sim$2.3 mag and $\sim$2 mag for $M^\star_{\mathrm{FUV}}$ and $M^\star_{\mathrm{NUV}}$, respectively, between $z \sim 2.2$ and $z \sim 0.15$.

Table 2. Best-fitting Schechter parameters of the FUV, NUV, and *U*-band LFs and associated LDs.

FUV: single-Schechter function								
Redshift	* M_{lim} [a]		** $N_{gal}^{\rm fit}$		$M^{\star}_{\rm FUV}$ [a]	$\phi^{\star}$ [b]	α	log($\rho_{\rm FUV}$ [c])
	Deep	*Ultra-deep*	*Deep*	*Ultra-deep*				
$0.05 < z < 0.3$	-14.21	–	111 819	–	-18.269 ± 0.054	4.85 ± 0.35	-1.405 ± 0.019	$25.719^{+0.009}_{-0.012}$
$0.3 < z < 0.45$	-15.17	–	150 738	–	-18.572 ± 0.038	5.22 ± 0.25	-1.369 ± 0.017	$25.873^{+0.005}_{-0.006}$
$0.45 < z < 0.6$	-15.79	–	168 370	–	-18.797 ± 0.073	4.13 ± 0.50	-1.408 ± 0.053	$25.885^{+0.012}_{-0.014}$
$0.6 < z < 0.9$	-17.16	-16.34	265 051	17 888	-19.113 ± 0.041	4.40 ± 0.30	-1.402 ± 0.038	$26.048^{+0.009}_{-0.011}$
$0.9 < z < 1.3$	-18.02	-17.27	422 362	28 890	-19.554 ± 0.065	4.97 ± 0.57	-1.432 ± 0.068	$26.304^{+0.018}_{-0.022}$
$1.3 < z < 1.8$	-18.79	-17.80	305 245	36 289	-20.016 ± 0.074	3.20 ± 0.38	-1.446 ± 0.074	$26.317^{+0.022}_{-0.025}$
$1.8 < z < 2.5$	-19.67	-18.91	180 033	22 979	-20.261 ± 0.042	2.82 ± 0.11	-1.43	$26.355^{+0.005}_{-0.006}$
$2.5 < z < 3.5$	–	-19.73	–	54 089	-20.841 ± 0.046	1.69 ± 0.10	-1.43	$26.373^{+0.011}_{-0.013}$
NUV: single-Schechter function								
Redshift	* M_{lim} [a]		** $N_{gal}^{\rm fit}$		$M^{\star}_{\rm NUV}$ [a]	$\phi^{\star}$ [b]	α	log($\rho_{\rm NUV}$ [c])
	Deep	*Ultra-deep*	*Deep*	*Ultra-deep*				
$0.05 < z < 0.3$	-14.38	–	117 326	–	-18.514 ± 0.025	5.08 ± 0.2	-1.399 ± 0.011	$25.847^{+0.006}_{-0.006}$
$0.3 < z < 0.45$	-15.37	–	157 999	–	-18.798 ± 0.03	6.01 ± 0.26	-1.308 ± 0.014	$26.009^{+0.007}_{-0.008}$
$0.45 < z < 0.6$	-16.02	–	174 053	–	-19.026 ± 0.062	4.56 ± 0.47	-1.364 ± 0.043	$26.009^{+0.009}_{-0.013}$
$0.6 < z < 0.9$	-17.27	-16.49	297 674	17 545	-19.416 ± 0.053	4.24 ± 0.4	-1.396 ± 0.044	$26.159^{+0.008}_{-0.010}$
$0.9 < z < 1.3$	-18.25	-17.49	404 623	28 462	-19.859 ± 0.052	4.7 ± 0.43	-1.385 ± 0.046	$26.385^{+0.009}_{-0.01}$
$1.3 < z < 1.8$	-19.13	-18.14	293 618	34 610	-20.367 ± 0.045	3.13 ± 0.23	-1.391 ± 0.038	$26.422^{+0.006}_{-0.008}$
$1.8 < z < 2.5$	-20.05	-19.24	173 206	23 007	-20.622 ± 0.034	2.72 ± 0.08	-1.4	$26.472^{+0.004}_{-0.004}$
$2.5 < z < 3.5$	–	-20.15	–	23 598	-21.152 ± 0.038	1.71 ± 0.11	-1.4	$26.489^{+0.015}_{-0.017}$
U-band: single-Schechter function								
Redshift	* M_{lim} [a]		** $N_{gal}^{\rm fit}$		$M^{\star}_{U,\ \rm Sing}$ [a]	$\phi^{\star}$ [b]	α	log($\rho_{U,\rm Sing}$ [c])
	Deep	*Ultra-deep*	*Deep*	*Ultra-deep*				
$0.05 < z < 0.3$	-15.17	–	121 413	–	-19.865 ± 0.030	3.60 ± 0.12	-1.424 ± 0.007	$26.291^{+0.004}_{-0.005}$
$0.3 < z < 0.45$	-16.20	–	155 008	–	-20.042 ± 0.020	5.62 ± 0.13	-1.22 ± 0.008	$26.466^{+0.003}_{-0.003}$
$0.45 < z < 0.6$	-16.86	–	166 133	–	-20.125 ± 0.017	5.05 ± 0.11	-1.178 ± 0.009	$26.439^{+0.002}_{-0.002}$
$0.6 < z < 0.9$	-17.91	-17.22	356 389	13 958	-20.435 ± 0.012	5.28 ± 0.08	-1.154 ± 0.008	$26.576^{+0.002}_{-0.002}$
$0.9 < z < 1.3$	-18.92	-18.21	461 661	24 246	-20.841 ± 0.014	4.66 ± 0.09	-1.251 ± 0.01	$26.723^{+0.002}_{-0.002}$
$1.3 < z < 1.8$	-19.74	-18.85	354 083	29 295	-21.241 ± 0.017	2.96 ± 0.07	-1.352 ± 0.013	$26.737^{+0.004}_{-0.004}$
$1.8 < z < 2.5$	–	-20.32	–	30 689	-21.677 ± 0.039	2.2 ± 0.12	-1.394 ± 0.033	$26.808^{+0.011}_{-0.011}$

U-band: double-Schechter function						
Redshift	$M^{\star}_{U,\ \rm Doub}$ [a]	$\phi_1^{\star}$ [b]	α_1	$\phi_2^{\star}$ [b]	α_2	log($\rho_{U,\ \rm Doub}$ [c])
$0.05 < z < 0.3$	-18.961 ± 0.050	3.4 ± 0.36	-1.568 ± 0.024	7.16 ± 0.25	-0.213 ± 0.099	$26.301^{+0.003}_{-0.003}$
$0.3 < z < 0.45$	-19.500 ± 0.040	2.41 ± 0.47	-1.557 ± 0.051	7.91 ± 0.3	-0.419 ± 0.092	$26.479^{+0.002}_{-0.003}$
$0.45 < z < 0.6$	-19.744 ± 0.027	1.96 ± 0.08	-1.56	5.59 ± 0.12	-0.506 ± 0.043	$26.452^{+0.002}_{-0.002}$
$0.6 < z < 0.9$	-20.244 ± 0.023	1.46 ± 0.11	-1.56	5.04 ± 0.09	-0.773 ± 0.042	$26.588^{+0.002}_{-0.002}$
$0.9 < z < 1.3$	-20.819 ± 0.033	0.51 ± 0.63	-1.56	4.28 ± 0.47	-1.187 ± 0.092	$26.727^{+0.014}_{-0.001}$

* Absolute magnitude completeness limits of the deep and ultra-deep layers (see equation 7).

**Number of galaxies with $M < M_{\rm lim}$ from the deep and ultra-deep layers used for fitting.

[a]AB mag.

[b]10^{-3} Mpc^{-3}.

[c]erg Hz^{-1} s^{-1} Mpc^{-3}.

Regarding the *U*-band Schechter parameters, it is relevant to consider both the single- and the double-Schechter parametric forms, since our data are deep enough to allow us to observe a double-Schechter profile which has not been documented and discussed in the literature so far. When considering the single-Schechter parameters, the slope α and normalization $\phi^{\star}$ appear particularly stable across cosmic time since $z \sim 1.6$, with $-1.4 \leq \alpha \leq -1.3$ and $\phi^{\star} = 3.0$–5.0×10^{-3} Mpc^{-3}; concurrently, $M^{\star}_{U,\ \rm Sing}$ fades by $\sim$1.3 mag. However, a single Schechter may not be appropriate for the *U*-band LF, since – as we discussed in the previous section – the double Schechter appears to better fit the *U*-band LF measured at $0.05 < z \leq 1.8$.

When considering a double Schechter, the dispersion observed in the faint-end slope of the *U*-band LF is slightly larger, with $-1.70 \leq \alpha_1 \leq -1.44$ at $0.05 < z \leq 0.6$ (where we let α_1 vary without any constraint except $\alpha_1 < \alpha_2$) and $-1.80 \leq \alpha_1 \leq -1.44$ at $0.05 < z \leq 1.8$. At the same time, the normalization of the faint end appears stable, increasing slightly from $\phi_1^{\star} = 1.0 \times 10^{-3}$ to 3.0×10^{-3}

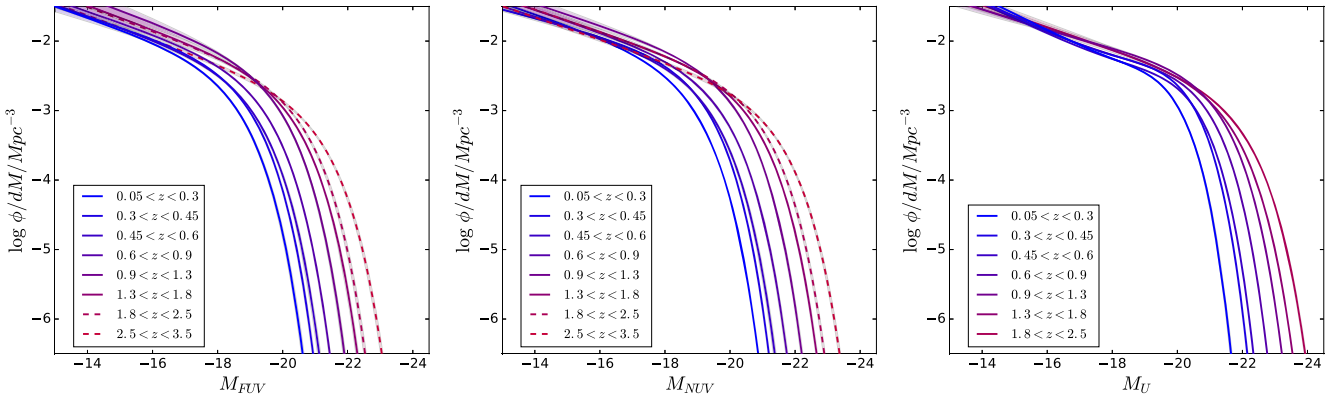

Figure 6. Redshift evolution of the FUV, NUV, and *U*-band LFs. Only the LF Schechter-based parametric form and corresponding 1σ uncertainty are shown here, with (solid and dashed) curves and associated envelopes, respectively. Dashed curves show Schechter-based fits with slopes that were not free to vary (see the text).

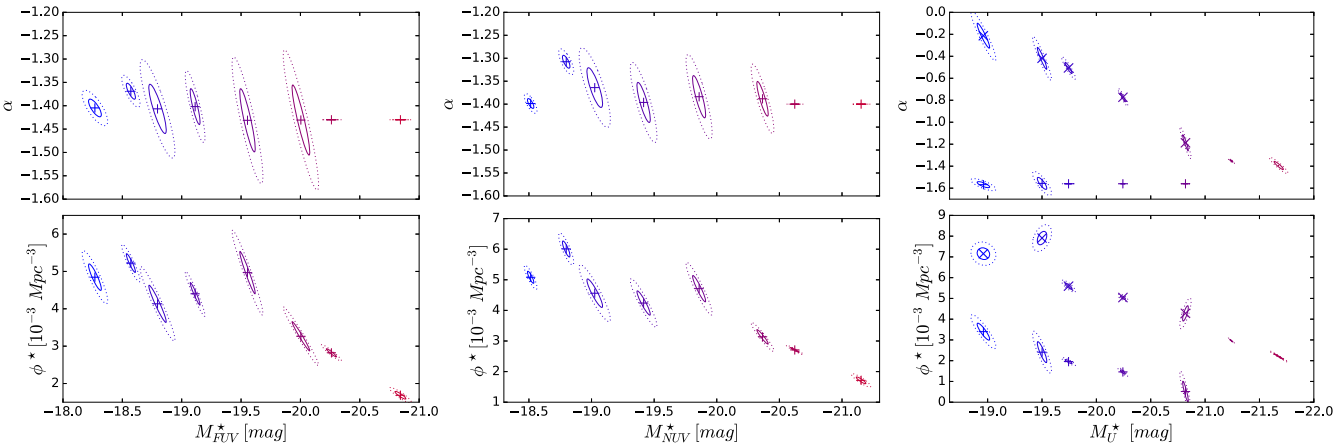

Figure 7. FUV, NUV, and *U*-band LF best-fitting Schechter parameters α and $\phi^\star$ as a function of $M^\star$ (crosses), and associated 1σ and 2σ confidence regions (solid and dotted ellipses, respectively). Consistently with the fitting procedure described in Section 3.2.2, the *U*-band LF Schechter parameters shown in the right-hand panel are those of a single-Schechter function at $1.3 < z < 2.5$, and a double-Schechter function at $0.05 < z < 1.3$: the faint-end component parameters (α_1, $\phi_1^\star$) and bright-end component parameters (α_2, $\phi_2^\star$) are shown with '+' and '×', respectively.

Mpc^{-3}. At the bright end, $-0.60 \leq \alpha_2 \leq -0.20$ at $0.05 < z \leq 0.6$ and $-0.70 \leq \alpha_2 \leq -0.20$ at $0.05 < z \leq 1.8$, while $\phi_2^\star$ increases from 4.1×10^{-3} to 7.3×10^{-3} Mpc^{-3} in the same redshift interval and the characteristic absolute magnitude $M^\star_{U,\ \mathrm{Doub}}$ fades by $\sim$1.7 mag.

While one may note that, on average, the double-Schechter parameters evolve in the same direction as the single-Schechter parameters, we note that the characteristic absolute magnitude depends substantially on the parametric form we adopted. In particular, the difference $|M^\star_{U,\ \mathrm{Doub}} - M^\star_{U,\ \mathrm{Sing}}|$ reaches $\sim$0.8 mag in our lowest redshift bin, i.e. where the faint-end upturn in the *U*-band LF is best probed. Considering a double-Schechter fit of the *U*-band LF is therefore imperative to compare our estimation of $M^\star_{\mathrm{U}}$ with other estimates based on shallower surveys.

3.2.4 Comparison with previous studies

Often simply referred to as the UV LF, the FUV LF has been extensively studied up to redshift $z \sim 9$, where rest-frame (not dust-corrected) UV can be constrained from mid-infrared observations. In Fig. 8, we compare our best-fitting Schechter parameters for the FUV LF with values from the literature across redshift. As one can see, our results are in overall good agreement with the literature at $0.05 < z \leq 3.5$. Given its unsurpassed combination of depth and area, our homogeneous data set provides the definitive reference measurement of the rest-frame FUV LF out to $z \sim 3$ at this time.

It is remarkable how well-behaved the values of the Schechter parameters are with redshift in Fig. 8 over the redshift range we measured them: $M^\star$ increases monotonically with lookback time, while both α and $\phi^\star$ remain essentially constant. The FUV LF slope α, which we measured directly from $z \sim 1.6$, is of particular interest, as it appears flatter than what is reported in the literature higher redshifts, from $z \sim 9$. This points to the existence of two regimes in the evolution of the FUV LF's faint end, which flattened from $z \sim 9$ before stabilizing at or before $z \sim 1.6$. Similarly, the evolution of $\phi^\star$ we measure is very stable from $z \sim 1.6$, and seem to be right in the middle of the literature values. At the same time, the continuous fading of the FUV LF's bright end characteristic absolute magnitude, $M^\star$ we observe from $z \sim 3$ is in line with the literature, though much better constrained with our data.

In contrast to the FUV LF, the NUV and *U*-band LFs are much less well documented in the literature, especially at $z > 1.5$. Fig. 9 shows our measurements of the NUV and *U*-band Schechter parameters compared with those from the literature. For the literature compilation, we only considered analyses where the

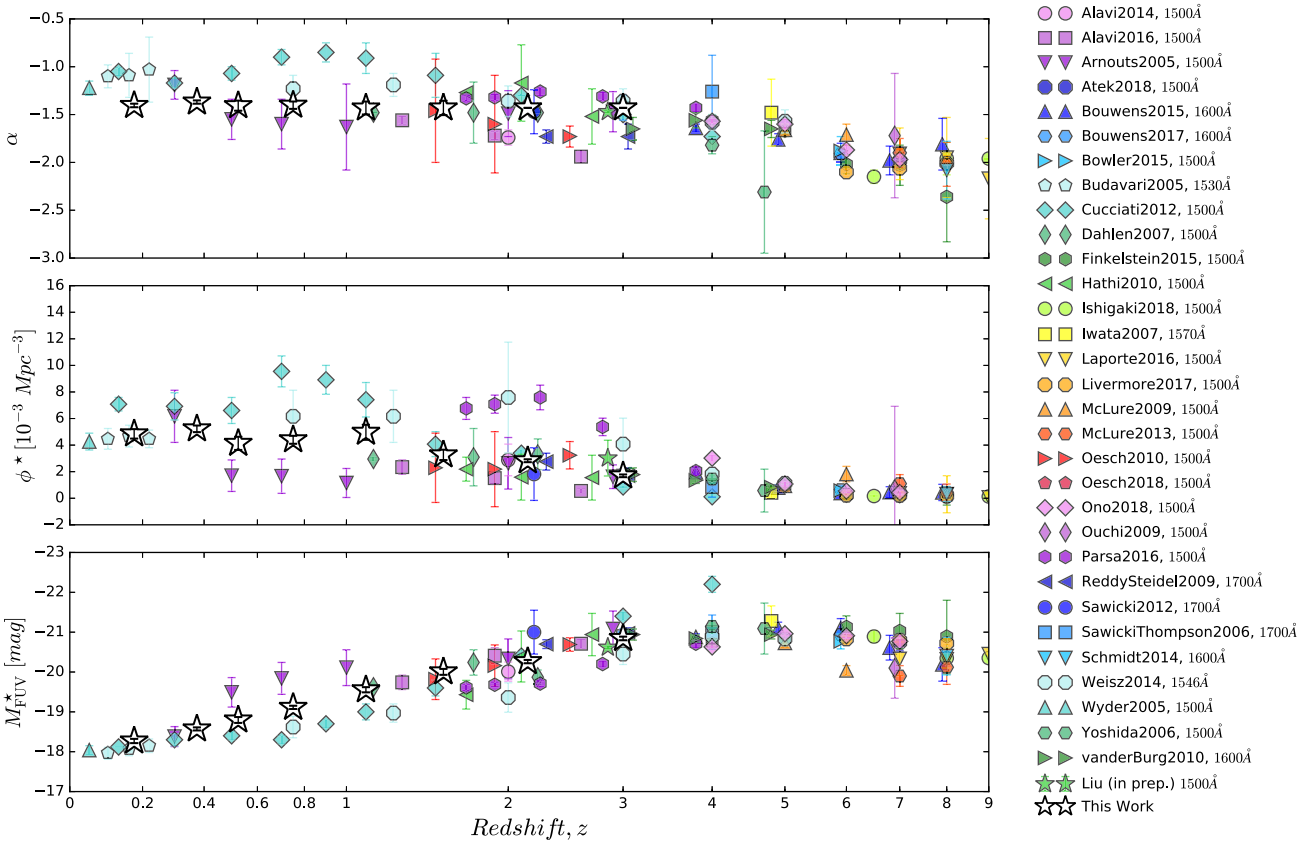

Figure 8. Comparison of the FUV Schechter parameters we found (open stars) with values compiled from the literature, namely Alavi et al. (2014), Alavi et al. (2016), Arnouts et al. (2005), Atek et al. (2018), Bouwens et al. (2015a), Bouwens et al. (2017), Bowler et al. (2015), Budavári et al. (2005), Cucciati et al. (2012), Dahlen et al. (2007), Finkelstein et al. (2015), Hathi et al. (2010), Ishigaki et al. (2018), Iwata et al. (2007), Laporte et al. (2016), Livermore, Finkelstein & Lotz (2017), McLure et al. (2009), McLure et al. (2013b), Oesch et al. (2010), Oesch et al. (2018), Ono et al. (2018), Ouchi et al. (2009), Parsa et al. (2016), Reddy & Steidel (2009b), Sawicki & Thompson (2006a), Sawicki (2012), Schmidt et al. (2014), Weisz, Johnson & Conroy (2014), Wyder et al. (2005), Yoshida et al. (2006), van der Burg et al. (2010), and Liu et al. (in preparation; light green stars), who used the same CLAUDS+HSC observations we used but based their LF measurements on *u*-dropouts.

parameters were free to vary over the redshift range covered by the literature, i.e. up to $z \sim 1.5$.

Our NUV LF Schechter parameters are in overall good agreement with the literature, but provide measurements that are much less noisy. This is particularly clear for the redshift dependence of α (and to a lower extent for $\phi^\star$), for which our measurement is more stable than what is found in the literature. Our α values, in particular, show a remarkable stability with redshift. At the same time, the evolution of $M^\star_{\rm NUV}$ we measured is in very good agreement with the literature, although even less noisy; with our excellent statistics, it shows a remarkably steady progression with cosmic time.

For the *U*-band LF, the comparison with the literature is different if we consider the single- or double-Schechter function fit. When considering a single-Schechter (star symbols in Fig. 9), the agreement with the literature is particularly good, especially for α and $\phi^\star$, while one may notice a little discrepancy for $M^\star_{\rm U}$ at $z < 0.5$. This is expected as the faint-end excess of galaxies in the *U*-band LF is more pronounced at low redshift, which directly affects our estimation of $M^\star_U$ due to the well-known degeneracy between the Schechter parameters α and $M^\star$ (as observed in Fig. 7). Thus, $M^\star_{U,\rm Doub}$ is in overall good agreement with the literature from $z \sim 0$ up to $z \sim 1$ (i.e. over all the redshift range where the comparison is possible), while exhibiting a much less noisy evolution.

3.3 Redshift evolution of the LDs

3.3.1 LD from the LF

In principle, the LD is obtained by summing the light from all the galaxies in unit volume. In practice, the LD can be estimated by integrating the LF. The LD of galaxies with luminosity greater than *L* is defined by

$$\rho(L) = \int_L^\infty L'\,\phi(L')\,{\rm d}L'. \quad (15)$$

If the LF has the (single-) Schechter form, this reduces to

$$\rho(L) = \phi^\star\ L^\star\ \Gamma(\alpha+2, L/L^\star), \quad (16)$$

where Γ is upper incomplete gamma function. In the case of a double-Schechter LF, equation (15) becomes

$$\rho(L) = L^\star\ \left[\ \phi_1^\star\ \Gamma(\alpha_1+2, L/L^\star) + \ \phi_2^\star\ \Gamma(\alpha_2+2, L/L^\star)\ \right]. \quad (17)$$

We derive the rest-frame FUV, NUV, and *U*-band LDs using the Schechter parameters we obtained in Section 3.2 and equation (16) or (17), as appropriate. We integrate over luminosity from ∞ down to $M_{\rm FUV}$, $M_{\rm NUV}$, $M_{\rm U} = -15$ to avoid heavy extrapolations. This limit is $\geq$3 mag below $M^\star$ for all of our LF measurements, and – given our relatively shallow values of α – it therefore captures the vast bulk of the luminosity that escapes the galaxy population. We

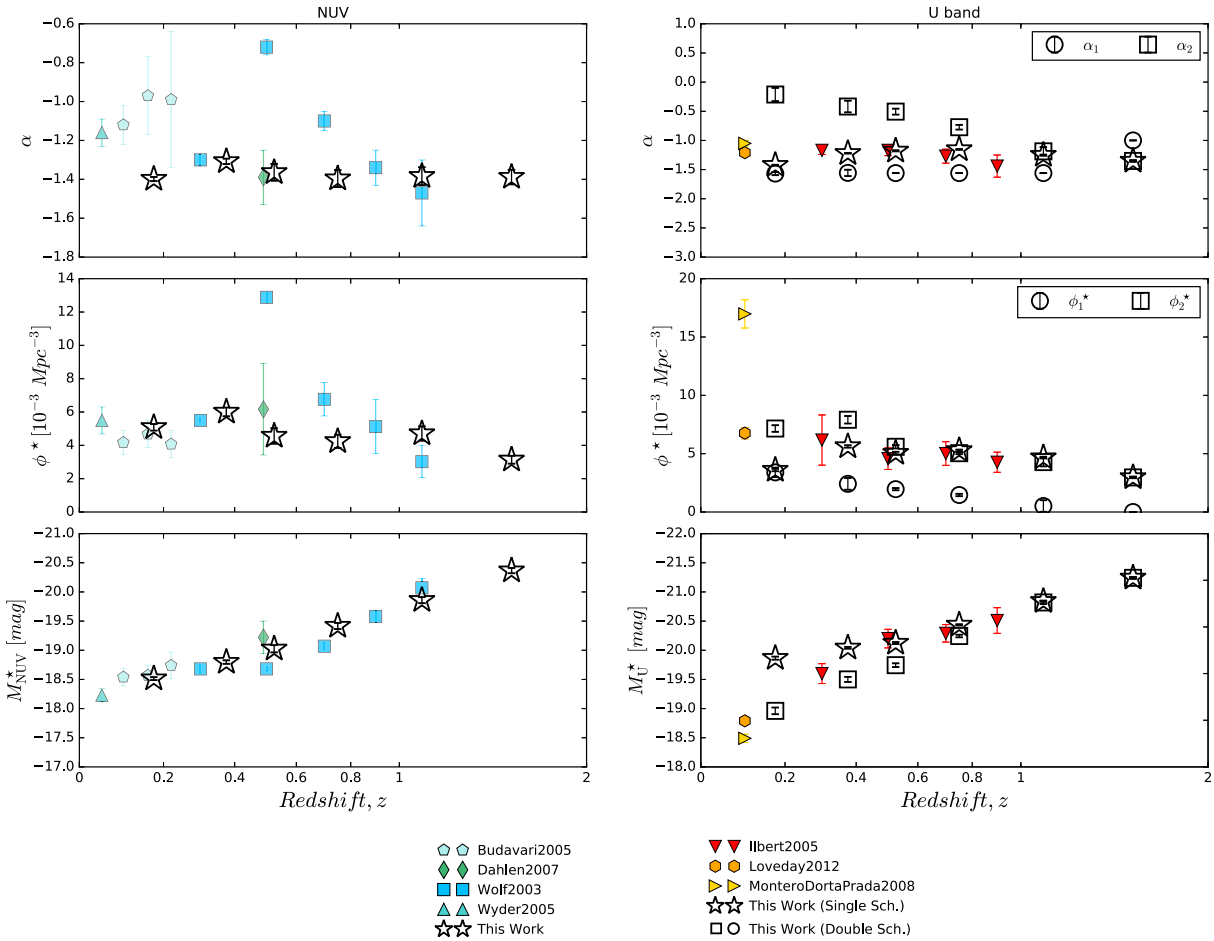

Figure 9. Comparison of the NUV and *U*-band (single-)Schechter parameters (open stars) with the literature, namely Budavári et al. (2005), Dahlen et al. (2007), Wolf et al. (2003), Wyder et al. (2005), Ilbert et al. (2005), Loveday et al. (2012), and Montero-Dorta & Prada (2009). In the right-hand panel, the double-Schechter best-fitting parameters we obtained for the *U*-band LF are overplotted (open circles and squares).

present the resulting LD values in the last column of Table 2 and discuss the results in the next section.

3.3.2 *Redshift evolution of the FUV, NUV, and U-band LDs*

Figs 10 and 11 show the redshift evolution of our FUV, NUV, and *U*-band LDs measured as described in Section 3.3.1. For comparison, we show LD values we recalculated from literature LF measurements for the same luminosity limits as those we applied to the CLAUDS+HSC-SSP data.

In Fig. 10, one can see how our results support a picture where the FUV LD has continuously decreased from $\rho_{\rm FUV} \sim 10^{26.35}$ down to $\sim 10^{25.7}$ erg s^{-1} Hz^{-1} Mpc^{-3} between $z \sim 2$ and $z \sim 0.2$ in good agreement with the literature. At the same time, our results show $\rho_{\rm FUV}$ to be stable at $1 \lesssim z \lesssim 2$ (and even at $1 \lesssim z \lesssim 3$ if we assume that the slope of $\alpha = -1.43$ we have set at $z > 1.8$ from lower-z measurements is correct). In that respect, our results appear to be consistent with a picture where the cosmic UV LD experienced a relatively stable phase before decreasing exponentially from redshift $z \sim 1$.

In Fig. 11(a), one can see a similar trend for the redshift evolution of the NUV LD, with a continuous decrease from $\rho_{\rm NUV} \sim 10^{26.4}$ down to $\sim 10^{25.85}$ erg s^{-1} Hz^{-1} Mpc^{-3} between $z \sim 1$ and $z \sim 0.2$, after a less pronounced evolution at $1 \lesssim z \lesssim 2$ (and also at $1 \lesssim z \lesssim 3$, assuming a slope of $\alpha = -1.4$ at $z > 1.8$). The evolution of the *U*-band LD shows a similar trend, at least at $z < 2$, with a continuous decrease of from $\rho_U \sim 10^{26.8}$ down to $\sim 10^{26.25}$ erg s^{-1} Hz^{-1} Mpc^{-3} between $z \sim 2$ and $z \sim 0.2$ and a more stable evolution at $1 \lesssim z \lesssim 2$, irrespective of whether we consider the double- or single-Schechter fits of the U-band LF, with the difference $|\log(\rho_{U,\,\rm Doub}) - \log(\rho_{U,\,\rm Sing})| \lesssim 0.01$ dex. That is in fairly good agreement with the literature shown in Figs 11(a) and (b), although comparison is only possible up to $z \sim 1$ for $\rho_{\rm NUV}$ and $\rho_{\rm U}$. These results are in-broad agreement with the picture first presented by Sawicki et al. (1997), namely that of a broad plateau at $1 \lesssim z \lesssim 3.5$ followed by a steep decline from $z \sim 1$ to $z \sim 0$ (the latter first measured by Lilly et al. 1996).[6]

Our CLAUDS+HSC-SSP measurements (Section 3) show that the evolution of the FUV and NUV LDs out to $z \sim 1$ is primarily driven by changes in $M^\star$ rather than in the faint-end slope, α, or the number density of galaxies, $\phi^\star$. At higher redshifts, $z \gtrsim 1$, while $M^\star$ continues to brighten, $\phi^\star$ begins to drop, with the two effects balancing each other to give the much milder, evolution seen at $z \gtrsim 1$ in Figs 10 and 11(a). The interpretation is more complicated in

[6]The Sawicki et al. (1997) measurements were performed at rest-frame UV wavelengths, but then were extrapolated to rest-frame 3000 Å (roughly mid-way between the NUV and *U* band of this study) for homogeneity with the $z \lesssim 1$ measurements of Lilly et al. (1996).

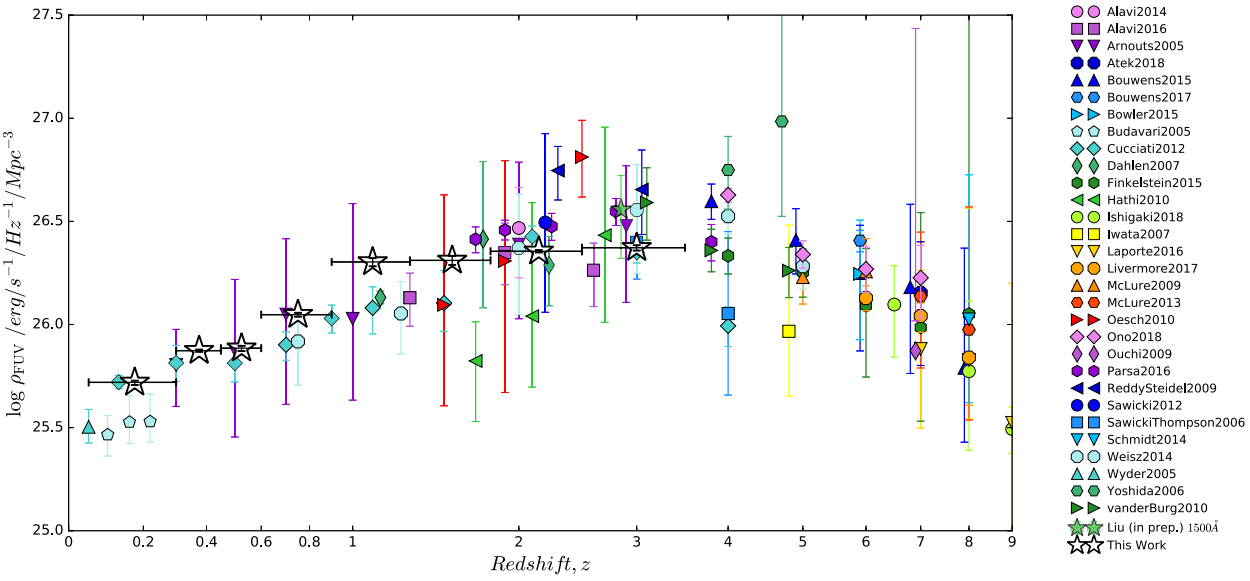

Figure 10. Redshift evolution of the FUV LDs for galaxies brighter than $M_{\rm FUV} = -15$ (open stars), and comparison with values derived from the literature, namely Alavi et al. (2014), Alavi et al. (2016), Arnouts et al. (2005), Atek et al. (2018), Bouwens et al. (2015a), Bouwens et al. (2017), Bowler et al. (2015), Budavári et al. (2005), Cucciati et al. (2012), Dahlen et al. (2007), Finkelstein et al. (2015), Hathi et al. (2010), Ishigaki et al. (2018), Iwata et al. (2007), Laporte et al. (2016), Livermore et al. (2017), McLure et al. (2009), McLure et al. (2013b), Oesch et al. (2010), Oesch et al. (2018), Ono et al. (2018), Ouchi et al. (2009), Parsa et al. (2016), Reddy & Steidel (2009b), Sawicki & Thompson (2006a), Sawicki (2012), Schmidt et al. (2014), Weisz et al. (2014), Wyder et al. (2005), Yoshida et al. (2006), van der Burg et al. (2010), and Liu et al. (in preparation; light green stars).

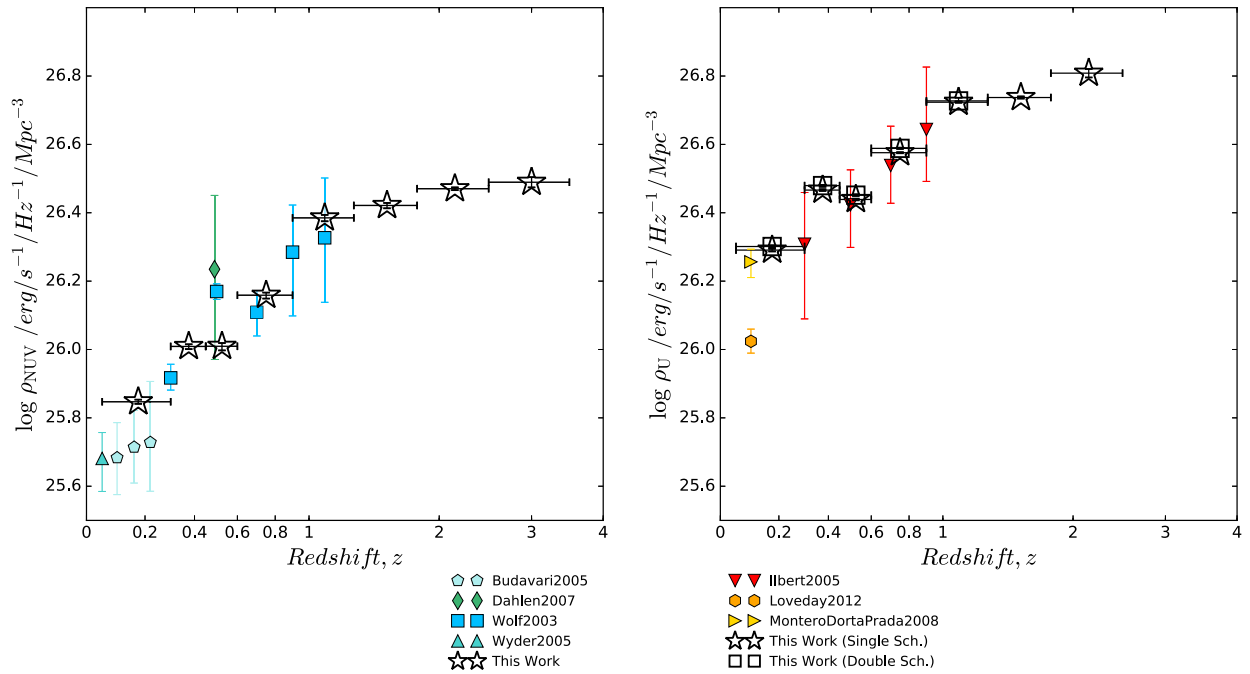

Figure 11. Redshift evolution of the NUV and U-band LDs for galaxies brighter than $M_{\rm NUV}$, $M_{\rm U} = -15$ (open stars), and comparison with values derived from the literature, namely Budavári et al. (2005), Dahlen et al. (2007), Wolf et al. (2003), Wyder et al. (2005), Ilbert et al. (2005), Loveday et al. (2012), and Montero-Dorta & Prada (2009). In the right-hand panel, the U-band LD we derived assuming a single- ($\rho_{\rm U,\ Sing}$; open stars) and double ($\rho_{U,\ \rm Doub}$; open squares) Schechter-parametric forms are reported.

the rest-frame U band because of the double-Schechter form of the U-band LF. There, we suspect that the build-up of the population of quiescent galaxies may contribute to the LF (bright end) and LD, as we explore in a forthcoming companion paper (Moutard et al. in preparation).

4 SUMMARY

In this paper, we presented our measurements of the $0 < z \lesssim 3$ rest-frame FUV (1546 Å), NUV (2345 Å), and U-band (3690 Å) galaxy LFs and LDs using more than 4.3 million galaxies from the

CLAUDS and HSC-SSP surveys. The unprecedented combination of depth ($U \sim 27$) and area ($\sim$18 deg^2) of this data set allows us to constrain the shape and evolution of these LFs with unmatched statistical precision and essentially free of cosmic variance.

The main results of this paper are the LF and LD measurements presented in the figures and tables in Section 3. In addition to these main products, we wish to highlight again the following observations:

(i) The rest-frame FUV and NUV LFs are described very well by the classic Schechter form over the full redshift range studied. The evolution of the Schechter parameters is very smooth with redshift. In particular, the values of $M^\star$ for both the FUV and NUV increase monotonically with increasing redshift, while the faint-end slopes are very stable up to $z \sim 2$, with slope values conservatively within $-1.42 \leq \alpha_{\rm FUV} \leq -1.31$ and $-1.53 \leq \alpha_{\rm NUV} \leq -1.28$ over $0.05 < z \leq 1.3$.

(ii) In contrast to the FUV and NUV LFs, the rest-frame U-band LFs are best described by a double-Schechter model, $M^\star_{U,\ \rm Doub}$, $\phi^\star_{U,1}$, $\phi^\star_{U,2}$, and $\alpha_{U,1}$ evolving continuously through $0.2 < z < 2$, assuming that $\alpha_{U,2}$ is simultaneously stable with redshift, which is confirmed to at least $z \sim 0.5$ (we are unable to measure it independently beyond this redshift). We speculate that the second-Schechter component in the rest-frame U-band LF is due to the population of quiescent galaxies – a topic we are currently investigating in a companion paper (Moutard in preparation).

(iii) We measured the rest-frame FUV, NUV, and U-band LDs by integrating the corresponding LFs down to $M = -15$ at $z \sim 0.2$. At all three wavelengths, we confirm previous results but with much better statistical precision afforded by our wide-and-deep CLAUDS+HSC-SSP data set: at all three rest wavelengths, the LD increases monotonically and rapidly with lookback time from $z \sim 0.2$ to $z \sim 1$ and then flattens to a much gentler slope at $z > 1$.

(iv) The very shallow evolution of the FUV and NUV LDs from $z \sim 3$ to $z \sim 1$ is driven by two competing effects acting within the LFs: the fading of the characteristic magnitude $M^\star$, which is balanced by the increase in the number of objects, $\phi^\star$ to produce the essentially flat LDs we observe over this wavelength range. At $z < 1$, the rapid evolution of the LDs is essentially due to the continuing fading of $M^\star$ only as both $\phi^\star$ and α remain essentially constant from $z \sim 1$ to $z \sim 0.2$.

We hope that the $0 < z < 3$ LF and LD measurements, we presented in this paper will serve as a useful reference to the community for making observational forecasts and validating theoretical models. In the future, we plan to extend the range of our LF and LD measurements to higher redshifts ($0 < z < 7$) by incorporating Lyman Break Galaxy LFs that we plan to do in a consistent way across this redshift range.

ACKNOWLEDGEMENTS

We gratefully acknowledge the anonymous reviewer, whose insightful comments helped in improving the clarity of the paper. We thank the CFHT observatory staff for their hard work in obtaining these data. The observations presented here were performed with care and respect from the summit of Maunakea which is a significant cultural and historic site. We thank Guillaume Desprez and Chengze Liu for helpful suggestions.

This work is based on observations obtained with MegaPrime/MegaCam, a joint project of CFHT and CEA/DAPNIA, at the CFHT which is operated by the National Research Council (NRC) of Canada, the Institut National des Science de l'Univers of the Centre National de la Recherche Scientifique (CNRS) of France, and the University of Hawaii. This research uses data obtained through the Telescope Access Program (TAP), which has been funded by the National Astronomical Observatories, Chinese Academy of Sciences, and the Special Fund for Astronomy from the Ministry of Finance. This work uses data products from TERAPIX and the Canadian Astronomy Data Centre. It was carried out using resources from Compute Canada and Canadian Advanced Network For Astrophysical Research (CANFAR) infrastructure. These data were obtained and processed as part of CLAUDS, which is a collaboration between astronomers from Canada, France, and China described in Sawicki et al. (2019).

This work is also based in part on data collected at the Subaru Telescope and retrieved from the HSC data archive system, which is operated by the Subaru Telescope and Astronomy Data Center at National Astronomical Observatory of Japan. The Hyper Suprime-Cam (HSC) collaboration includes the astronomical communities of Japan and Taiwan, and Princeton University. The HSC instrumentation and software were developed by the National Astronomical Observatory of Japan (NAOJ), the Kavli Institute for the Physics and Mathematics of the Universe (Kavli IPMU), the University of Tokyo, the High Energy Accelerator Research Organization (KEK), the Academia Sinica Institute for Astronomy and Astrophysics in Taiwan (ASIAA), and Princeton University. Funding was contributed by the FIRST programme from Japanese Cabinet Office, the Ministry of Education, Culture, Sports, Science and Technology (MEXT), the Japan Society for the Promotion of Science (JSPS), Japan Science and Technology Agency (JST), the Toray Science Foundation, NAOJ, Kavli IPMU, KEK, ASIAA, and Princeton University. This paper makes use of software developed for the Large Synoptic Survey Telescope. We thank the LSST Project for making their code available as free software at http://dm.lsst.org.

This work was financially supported by a Discovery Grant from the Natural Sciences and Engineering Research Council (NSERC) of Canada, by the Programme National Cosmology et Galaxies (PNCG) of CNRS/INSU with INP and IN2P3, and by the Centre National d'Etudes Spatiales (CNES).

REFERENCES

Aihara H. et al., 2018a, PASJ, 70, S8
Aihara H. et al., 2018b, PASJ, 70, S4
Aihara H. et al., 2019, preprint (arXiv:1905.12221)
Alavi A. et al., 2014, ApJ, 780, 143
Alavi A. et al., 2016, ApJ, 832, 56
Andrae R., Schulze-Hartung T., Melchior P., 2010, preprint (arXiv:1012.3754)
Arnouts S. et al., 2002, MNRAS, 329, 355
Arnouts S. et al., 2005, ApJ, 619, L43
Atek H., Richard J., Kneib J.-P., Schaerer D., 2018, MNRAS, 479, 5184
Bertin E., Arnouts S., 1996, A&AS, 117, 393
Bouwens R. J. et al., 2009, ApJ, 705, 936
Bouwens R. J. et al., 2012, ApJ, 754, 83
Bouwens R. J. et al., 2015a, ApJ, 803, 34
Bouwens R. J., Illingworth G. D., Oesch P. A., Caruana J., Holwerda B., Smit R., Wilkins S., 2015b, ApJ, 811, 140
Bouwens R. J. et al., 2016, ApJ, 830, 67
Bouwens R. J., Oesch P. A., Illingworth G. D., Ellis R. S., Stefanon M., 2017, ApJ, 843, 129
Bowler R. A. A. et al., 2015, MNRAS, 452, 1817
Bradshaw E. J. et al., 2013, MNRAS, 433, 194
Bruzual G., Charlot S., 2003, MNRAS, 344, 1000
Budavári T. et al., 2005, ApJ, 619, L31

Caputi K. I., Cirasuolo M., Dunlop J. S., McLure R. J., Farrah D., Almaini O., 2011, MNRAS, 413, 162
Chabrier G., 2003, PASP, 115, 763
Chapman S. C., Blain A. W., Smail I., Ivison R. J., 2005, ApJ, 622, 772
Comparat J. et al., 2015, A&A, 575, A40
Conroy C., 2013, ARA&A, 51, 393
Conseil S., Vibert D., Amouts S., Milliard B., Zamojski M., Liebaria A., Guillaume M., 2011, in Evans I. N., Accomazzi A., Mink D. J., Rots A. H., eds, ASP Conf. Ser. Vol. 442, Astronomical Data Analysis Software and Systems XX. Astron. Soc. Pac., San Francisco, p. 107
Coupon J. et al., 2015, MNRAS, 449, 1352
Cucciati O. et al., 2012, A&A, 539, A31
Dahlen T., Mobasher B., Dickinson M., Ferguson H. C., Giavalisco M., Kretchmer C., Ravindranath S., 2007, ApJ, 654, 172
Davidzon I. et al., 2017, A&A, 605, A70
Eddington A. S., 1913, MNRAS, 73, 359
Efstathiou G., Ellis R. S., Peterson B. A., 1988, MNRAS, 232, 431
Finkelstein S. L. et al., 2015, ApJ, 810, 71
Goto T. et al., 2019, PASJ, 71, 30
Grazian A. et al., 2015, A&A, 575, A96
Gruppioni C. et al., 2013, MNRAS, 432, 23
Guillaume M., Llebaria A., Aymeric D., Arnouts S., Milliard B., 2006, in Dougherty E. R., Astola J. T., Egiazarian K. O., Nasrabadi N. M., Rizvi S. A., eds, SPIE Conf. Ser. Vol. 6064, Image Processing: Algorithms and Systems, Neural Networks, and Machine Learning. Astron. Soc. Pac., San Francisco, p. 332
Hathi N. P. et al., 2010, ApJ, 720, 1708
Henriques B. M. B., White S. D. M., Thomas P. A., Angulo R. E., Guo Q., Lemson G., Springel V., 2013, MNRAS, 431, 3373
Hildebrandt H. et al., 2012, MNRAS, 421, 2355
Hughes D. H. et al., 1998, Nature, 394, 7
Ilbert O. et al., 2005, A&A, 439, 863
Ilbert O. et al., 2006, A&A, 457, 841
Ilbert O. et al., 2009, ApJ, 690, 1236
Ilbert O. et al., 2013, A&A, 556, A55
Inoue A. K., Iwata I., Deharveng J.-M., 2006, MNRAS, 371, L1
Ishigaki M., Kawamata R., Ouchi M., Oguri M., Shimasaku K., Ono Y., 2018, ApJ, 854, 73
Iwata I., Ohta K., Tamura N., Akiyama M., Aoki K., Ando M., Kiuchi G., Sawicki M., 2007, MNRAS, 376, 1557
Iwata I., Inoue A. K., Micheva G., Matsuda Y., Yamada T., 2019, MNRAS, 488, 5671
Khusanova Y. et al., 2020, A&A, 634, A97
Kitzbichler M. G., White S. D. M., 2007, MNRAS, 376, 2
Kriek M. et al., 2015, ApJS, 218, 15
Kron R. G., 1980, ApJS, 43, 305
Lacey C. G., Baugh C. M., Frenk C. S., Benson A. J., 2011, MNRAS, 412, 1828
Lacey C. G. et al., 2016, MNRAS, 462, 3854
Laigle C. et al., 2016, ApJS, 224, 24
Laporte N. et al., 2016, ApJ, 820, 98
Leauthaud A. et al., 2007, ApJS, 172, 219
Leja J. et al., 2019, ApJ, 877, 140
Le Févre O. et al., 2013, A&A, 559, A14
Lilly S. J., Tresse L., Hammer F., Crampton D., Le Fevre O., 1995, ApJ, 455, 108
Lilly S. J., Le Fevre O., Hammer F., Crampton D., 1996, ApJ, 460, L1
Lilly S. J. et al., 2007, ApJS, 172, 70
Livermore R. C., Finkelstein S. L., Lotz J. M., 2017, ApJ, 835, 113
Loveday J. et al., 2012, MNRAS, 420, 1239
Madau P., Dickinson M., 2014, ARA&A, 52, 415
Madau P., Ferguson H. C., Dickinson M. E., Giavalisco M., Steidel C. C., Fruchter A., 1996, MNRAS, 283, 1388
Magnelli B. et al., 2013, A&A, 553, A132
Maraston C., 2005, MNRAS, 362, 799
Martin D. C. et al., 2005, ApJ, 619, L1
Maseda M. V., Franx M., Chevallard J., Curtis-Lake E., 2019, MNRAS, 486, 3290
Masters D. C., Stern D. K., Cohen J. G., Capak P. L., Rhodes J. D., Castander F. J., Paltani S., 2017, ApJ, 841, 111
Masters D. C. et al., 2019, ApJ, 877, 81
Matsuoka Y., Kawara K., 2010, MNRAS, 405, 100
McLure R. J., Cirasuolo M., Dunlop J. S., Foucaud S., Almaini O., 2009, MNRAS, 395, 2196
McLure R. J. et al., 2013a, MNRAS, 428, 1088
McLure R. J. et al., 2013b, MNRAS, 432, 2696
Meurer G. R., Heckman T. M., Lehnert M. D., Leitherer C., Lowenthal J., 1997, AJ, 114, 54
Mitchell P. D., Lacey C. G., Baugh C. M., Cole S., 2013, MNRAS, 435, 87
Montero-Dorta A. D., Prada F., 2009, MNRAS, 399, 1106
Moutard T. et al., 2016a, A&A, 590, A102
Moutard T. et al., 2016b, A&A, 590, A103
Muzzin A. et al., 2013, ApJ, 777, 18
Oesch P. A. et al., 2010, ApJ, 725, L150
Oesch P. A., Bouwens R. J., Illingworth G. D., Labbé I., Stefanon M., 2018, ApJ, 855, 105
Oke J., 1974, ApJS, 27, 21
Ono Y., et al., 2018, PASJ, 70, S10
Ouchi M. et al., 2004, ApJ, 611, 660
Ouchi M. et al., 2009, ApJ, 706, 1136
Papovich C., Dickinson M., Ferguson H. C., 2001, ApJ, 559, 620
Parsa S., Dunlop J. S., McLure R. J., Mortlock A., 2016, MNRAS, 456, 3194
Pozzetti L. et al., 2010, A&A, 523, A13
Reddy N. A., Steidel C. C., 2009a, ApJ, 692, 778
Reddy N. A., Steidel C. C., 2009b, ApJ, 692, 778
Salpeter E. E., 1955, ApJ, 121, 161
Sawicki M., 2012, MNRAS, 421, 2187
Sawicki M., Thompson D., 2006a, ApJ, 642, 653
Sawicki M., Thompson D., 2006b, ApJ, 648, 299
Sawicki M., Yee H. K. C., 1998, AJ, 115, 1329
Sawicki M. J., Lin H., Yee H. K. C., 1997, AJ, 113, 1
Sawicki M. et al., 2019, MNRAS, 489, 5202
Schechter P., 1976, ApJ, 203, 297
Schiminovich D. et al., 2005, ApJ, 619, L47
Schmidt M., 1968, ApJ, 151, 393
Schmidt K. B. et al., 2014, ApJ, 786, 57
Scodeggio M. et al., 2018, A&A, 609, A84
Scoville N. et al., 2007, ApJS, 172, 1
Sharma M., Theuns T., Frenk C., Bower R., Crain R., Schaller M., Schaye J., 2016, MNRAS: Letters, 458, L94
Silverman J. D. et al., 2015, ApJS, 220, 12
Somerville R. S., Gilmore R. C., Primack J. R., Domínguez A., 2012, MNRAS, 423, 1992
Sorba R., Sawicki M., 2015, MNRAS, 452, 235
Sorba R., Sawicki M., 2018, MNRAS, 476, 1532
Steidel C. C., Adelberger K. L., Giavalisco M., Dickinson M., Pettini M., 1999, ApJ, 519, 1
Tasca L. A. M. et al., 2017, A&A, 600, A110
van der Burg R. F. J., Hildebrandt H., Erben T., 2010, A&A, 523, A74
Weisz D. R., Johnson B. D., Conroy C., 2014, ApJ, 794, L3
Williams R. E. et al., 1996, AJ, 112, 1335
Williams C. C. et al., 2018, ApJS, 236, 33
Wolf C., Meisenheimer K., Rix H. W., Borch A., Dye S., Kleinheinrich M., 2003, A&A, 401, 73
Wyder T. K. et al., 2005, ApJ, 619, L15
Yoshida M. et al., 2006, ApJ, 653, 988

APPENDIX A: FITTING THE *U*-BAND LF

As observed in Figs 5 and B3, the *U*-band LF exhibits an upturn at the faint end, which results in a deviation from the shape of a

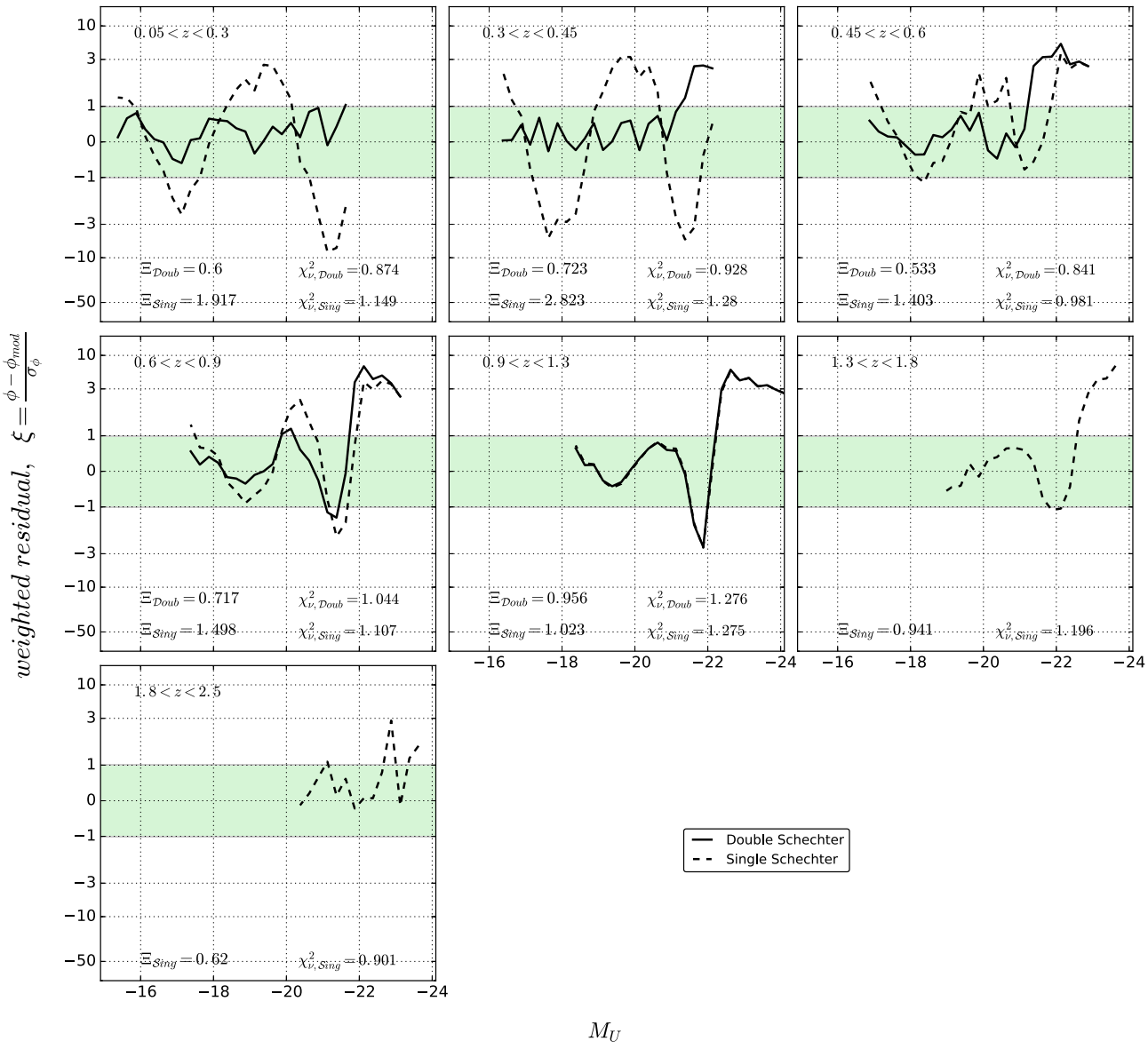

Figure A1. Weighted residuals ξ as a function as a function of the U-band absolute magnitude: for our single-Schechter (dashed lines) and double-Schechter (solid lines) models of the U-band LF. The green shaded area shows the region where the agreement between the model and the data is optimal (i.e. the residual is within the uncertainty), with $|\,\xi\,| = |\,\frac{\phi-\phi_{\rm mod}}{\sigma_\phi}\,| \leq 1$. The associated typical deviations of the model (see equation A2), $\Xi_{\rm Sing}$ and $\Xi_{\rm Doub}$, are reported in the lower left corner of the sub-panels. While not optimal to compare the goodness of fit of non-linear models with different numbers of free parameters (see Appendix A), the corresponding reduced χ^2 values are noted in the lower right corners, for information.

pure Schechter function and argues for fitting the U-band LF with a double-Schechter function.

In order to assess whether a double-Schechter function is quantitatively better adapted to the U-band LF, we need to compare the goodness of fit of two non-linear models with different numbers of parameters. While one might be inclined to compare the associated reduced χ^2, defined as $\chi^2_\nu = \chi^2/\nu$ (where ν is the number of degrees of freedom), ν is generally not of the commonly assumed form $\nu = N - M$ for non-linear models (Andrae, Schulze-Hartung & Melchior 2010). Consequently, the best way to compare the goodness of fit of single- and double-Schechter functions is actually to return to the distribution of the fit residuals.

To better appreciate the significance of the residual between the observed LF, ϕ, and its parametric form, $\phi_{\rm mod}$, it is relevant to consider the weighted residual, ξ, defined by

$$\xi = \frac{\phi - \phi_{\rm mod}}{\sigma_\phi}, \tag{A1}$$

where the residual $\phi - \phi_{\rm mod}$ is normalized by the LF uncertainty σ_ϕ. Thereby, at given absolute magnitude, good agreement between the model and the data is met when the residual is smaller than the statistical uncertainty, i.e. when $-1 \lesssim \xi \lesssim 1$ (or when $|\,\xi\,| \lesssim 1$). Then, aiming at characterizing the distribution of the residuals, it may be convenient to define $\Xi_{\rm mod}$ as the normalized median absolute deviation of the model $\phi_{\rm mod}$:

$$\begin{aligned}\Xi_{mod} &= 1.48 \times \text{median}\left(\left|\frac{\phi - \phi_{\rm mod}}{\sigma_\phi}\right|\right) \\ &= 1.48 \times \text{median}(|\xi|),\end{aligned} \tag{A2}$$

$\Xi_{\rm mod}$ being thereby a measure of the typical deviation of the model around the data relative to the statistical uncertainty on the data. In other words, there is overall good agreement of the model with the data when $\Xi_{\rm mod} \lesssim 1$ and the better agreement, the smaller $\Xi_{\rm mod}$ is.

In Fig. A1, we plotted the weighted residual as a function of the *U*-band absolute magnitude, $M_{\rm U}$, and we compare the residuals we obtained when fitting the LF with single- and double-Schechter functions. The typical deviation for the single- and double-Schechter fits, $\Xi_{\rm Sing}$ and $\Xi_{\rm Doub}$ are reported in the lower left corner of each sub-panel in Fig. A1, while the corresponding reduced χ^2 are reported in the lower right corners of the sub-panels for information.

As one can see, the advantage of using a double-Schechter function to fit the *U*-band LF is clear up to $z = 0.9$. Associated residuals are indeed smaller than the statistical uncertainty from the faint end (notably around $M_U \sim -17$ where the upturn is observed; see Fig. 5) to the bright end, before the disagreement start increasing around $M_U \sim -21.5$ due to Eddington bias (see Section 3.2.1) and contamination by stars and quasars (see Appendix C). One may notice that this translates into $\Xi_{\rm Doub} < 0.75$, which traces a pretty good agreement between the data and the best-fitting solution with a double-Schechter function, while the best single-Schechter solution is clearly worse, with $\Xi_{\rm Sing} > 1.4$ (i.e. $\Xi_{\rm Sing} \simeq 2$–$4 \times \Xi_{\rm Doub}$). At $0.9 < z < 1.3$, although single- and double-Schechter functions appear to provide similar results, the typical deviations of the two models tend to confirm that a double-Schechter profile better fits the *U*-band LF, with $\Xi_{\rm Doub} < 1 < \Xi_{\rm Sing}$. At higher redshifts, the completeness limits of our data ($M_{U,\rm lim} = -18.85$ and -20.32 at $1.3 < z < 1.8$ and $1.8 < z < 2.5$, respectively) prevent us from detecting any excess of galaxies at the faint end (the excess is typically visible for $M_U \gtrsim -17$ at lower redshift, as recalled above). No definitive conclusion can therefore be drawn about the relevance of fitting the *U*-band LF with a double-Schechter function at $z > 1.3$, where a simple Schechter function fits well the LF (for $M_U < M_{U,\rm lim}$), with $\Xi_{\rm Sing} < 1$.

APPENDIX B: VARIATION OF THE LFS FROM FIELD TO FIELD

Figs B1–B3 show, respectively, the FUV, NUV, and *U*-band raw LFs we measured in our eight redshift bins, for each of the four fields of our survey: DEEP2-3, ELAIS-N1, XMM-LSS, and E-COSMOS. In these figures, the deep and ultra-deep layers are not separated, which explains why XMM-LSS and E-COSMOS, which contain the ultra-deep layer, appear deeper than DEEP2-3 and ELAIS-N1.

The deviation between the LFs measured in each field illustrates the cosmic variance affecting the LF measurement in each field. One can see how the cosmic variance depends on the cosmic volume probed for a given redshift bin and a given effective area: it is thereby not surprising to observe the largest deviation between field LFs in our lowest redshift bin, $0.05 < z \leq 0.3$.

On the other hand, the deviation between the LFs one can observe from field to field at the extremely bright end, for very small comoving densities $<10^{-5}$ Mpc^{-3}, is likely to be due contamination by stars and QSOs that could not be discarded by the procedure described in Section 2.2. Indeed, the photometric identification of stars and QSOs depends on the SNR of the sources (i.e. the depth of the data), which is different in our different fields. In that respect, what can be seen in Fig. B3 at $0.9 < z \leq 1.3$ (where most of the *U*-band absolute magnitudes are derived from observed *i* band) is particularly striking but not surprising: XMM-LSS and E-COSMOS host indeed our ultra-deep layer and include much deeper *g*, *r*, *i*, *z*, *y* observations than DEEP2-3 and ELAIS-N1.

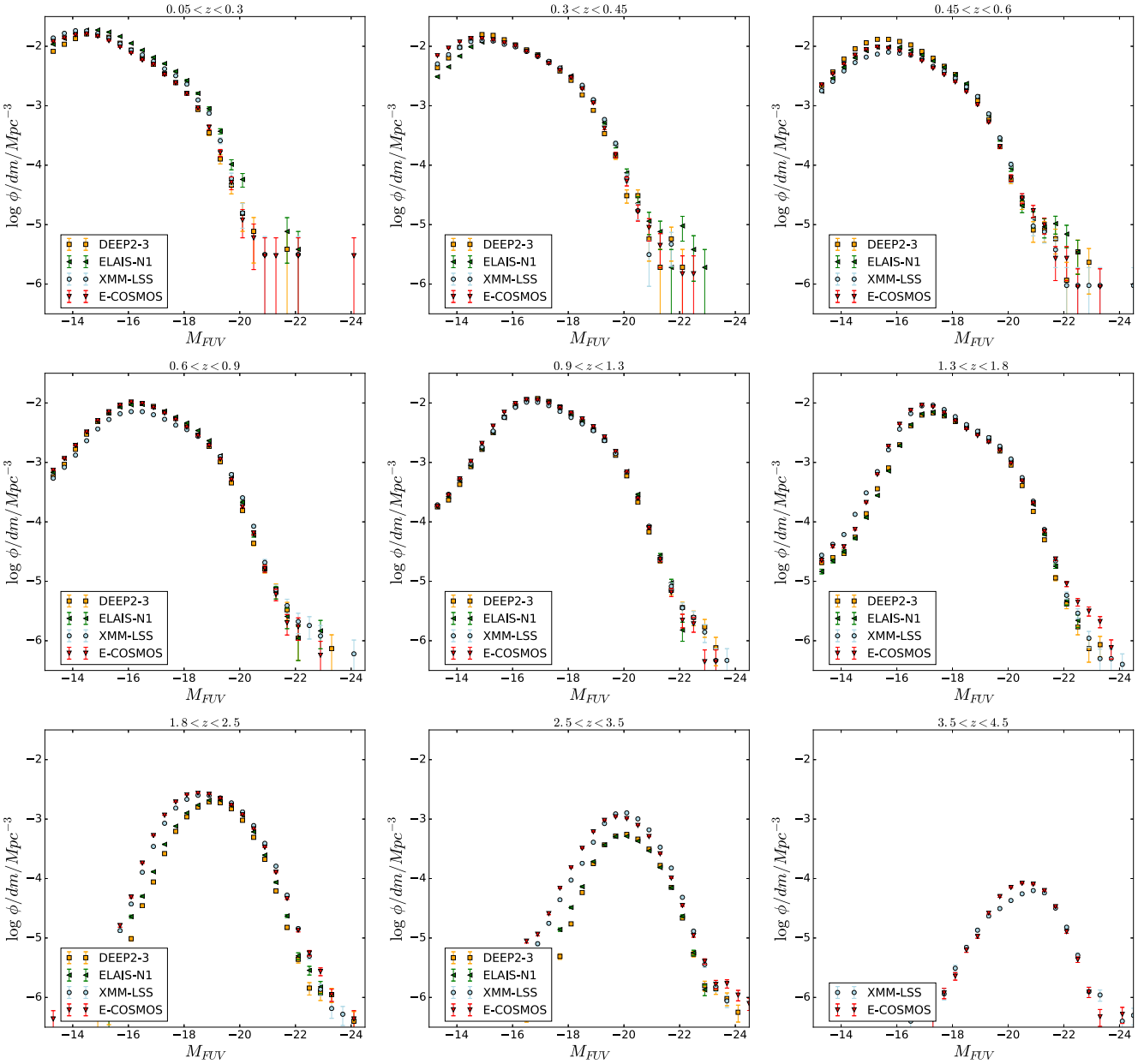

Figure B1. FUV LF in the four fields of CLAUDS+HSC: DEEP2-3, ELAIS-N1, XMM-LSS, and E-COSMOS.

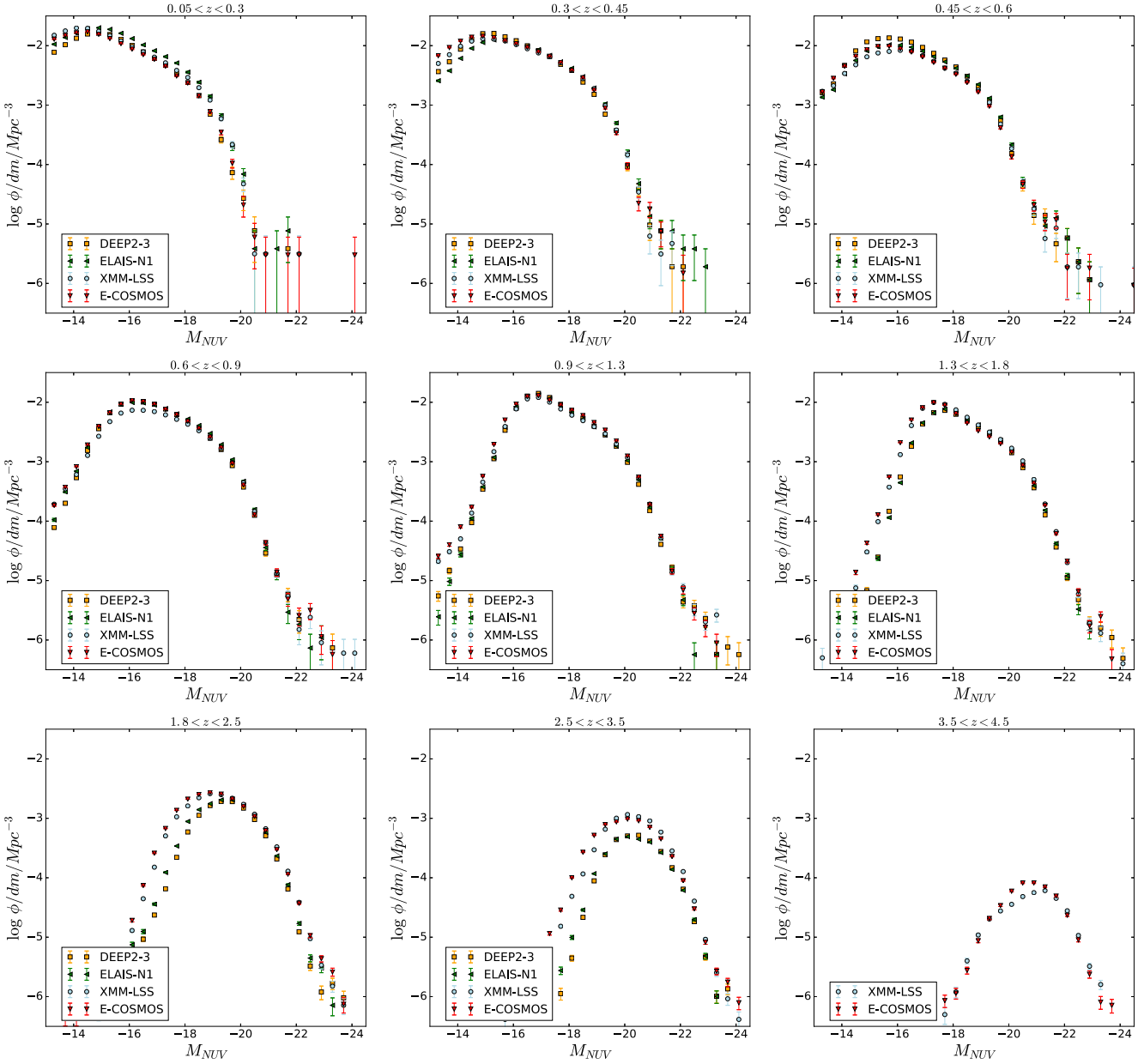

Figure B2. NUV LF in the four fields of CLAUDS+HSC: DEEP2-3, ELAIS-N1, XMM-LSS, and E-COSMOS.

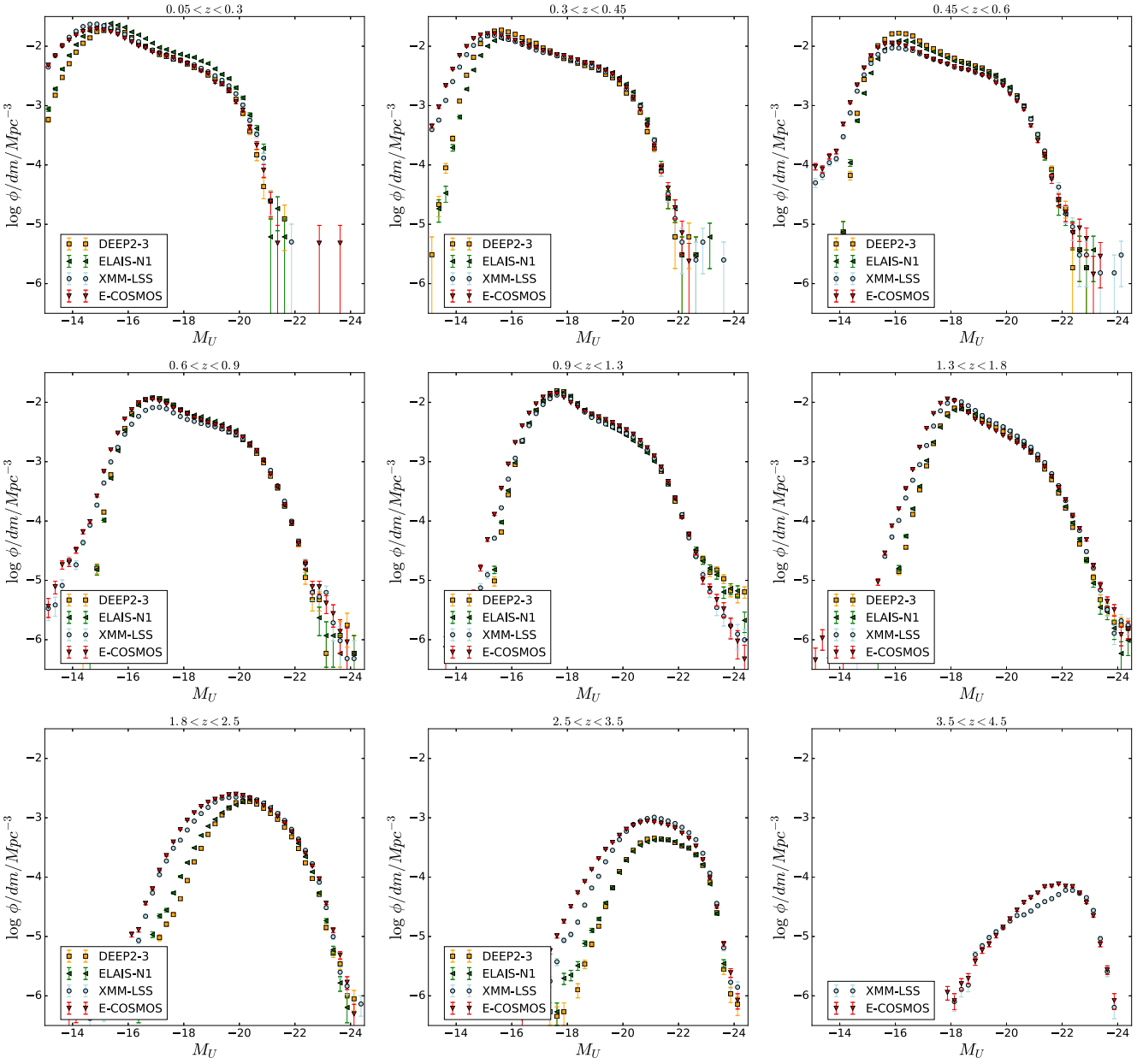

Figure B3. *U*-band LF in the four fields of CLAUDS+HSC: DEEP2-3, ELAIS-N1, XMM-LSS, and E-COSMOS.

APPENDIX C: LF PER TYPE OF SOURCE

Figs C1–C3 show, respectively, the FUV, NUV, and *U*-band LFs we could measure in our eight redshift bins, depending on the type of sources we identified with the procedure described in Section 2.2: galaxies, quasars, and stars.

Stars with $z > 0$ are obviously not real, and the redshifts of QSOs are most probably wrong, but the exercise allows us to see how and where these two populations may contaminate our LF measurements. Indeed, as one can see in all FUV, NUV, and *U*-band LFs, sources classified as stars and QSOs are completely dominated by the galaxy population at low luminosities (faint absolute magnitudes) down to the completeness limit, but their incidence increases with increasing luminosity to become as numerous as galaxies at the very bright end of the LFs.

This seems to confirm that the extremely bright end of our LF measurements may significantly suffer from contamination by stars and QSOs, typically for comoving densities $<10^{-5}$ Mpc^{-3}. None the less, we verified that this very limited population did not affect our analysis, as described in Section 3.2.1.

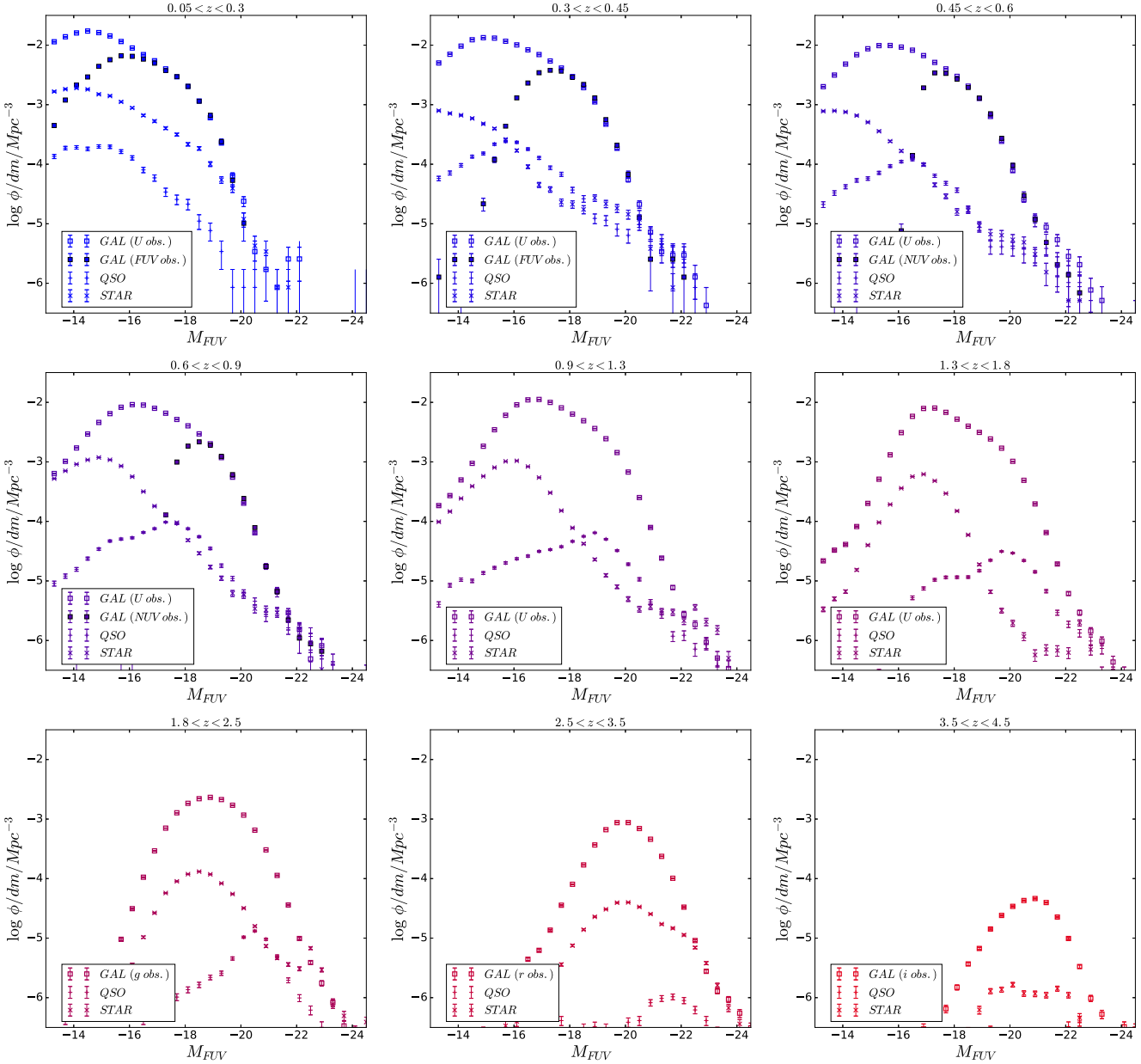

Figure C1. FUV LF of the different types of sources identified in our analysis: galaxies (GAL), quasars (QSO), and stars. The very bright end is mostly populated by stars and QSOs, which confirms that the deviation of the bright end of galaxy FUV LF from a pure Schechter form is likely to be due to contamination from stars and QSOs.

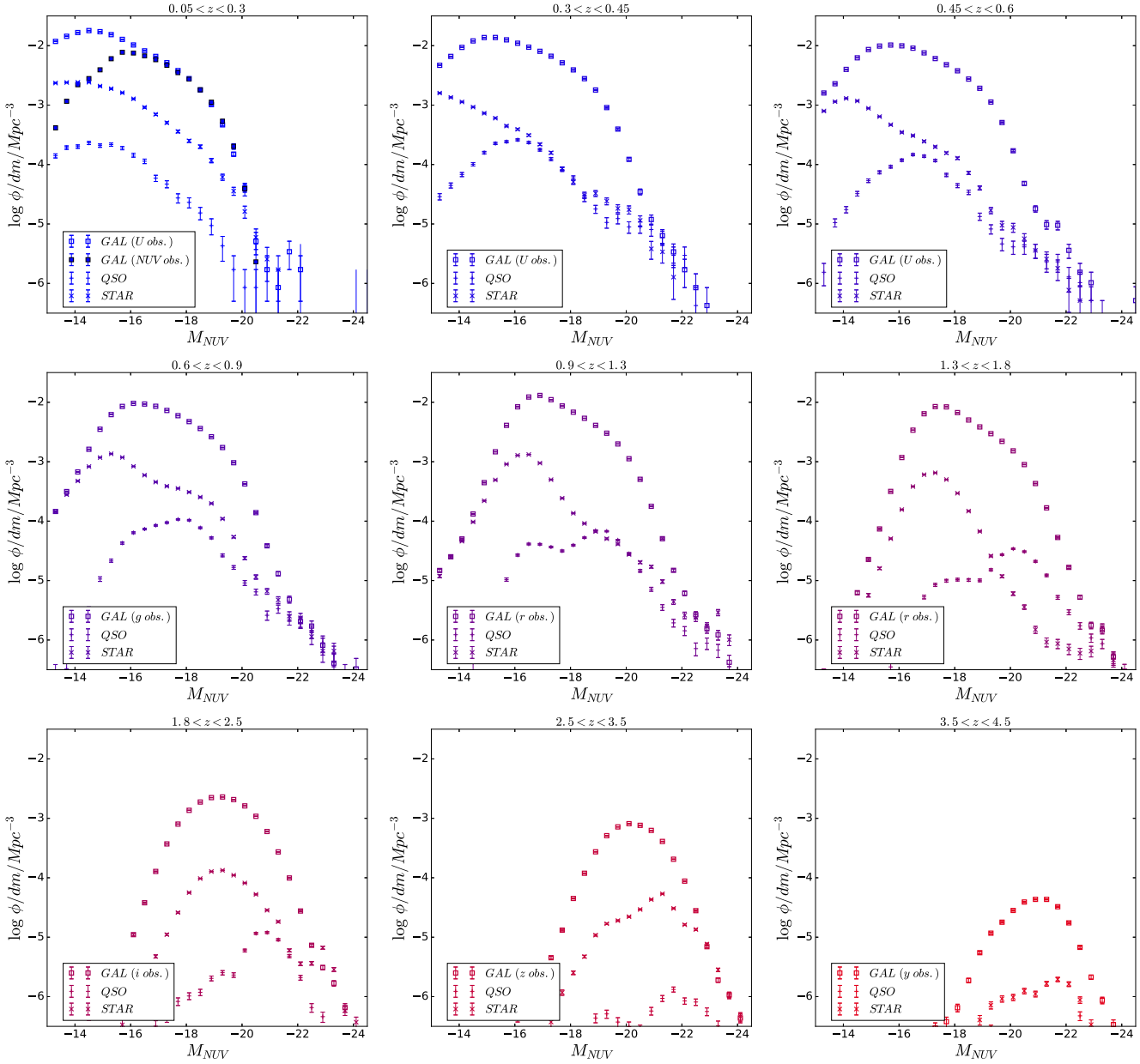

Figure C2. NUV LF of the different types of sources identified in our analysis: galaxies (GAL), quasars (QSO), and stars. The very bright end is mostly populated by stars and QSOs, which confirms that the deviation of the bright end of galaxy NUV LF from a pure Schechter form is likely to be due to contamination from stars and QSOs.

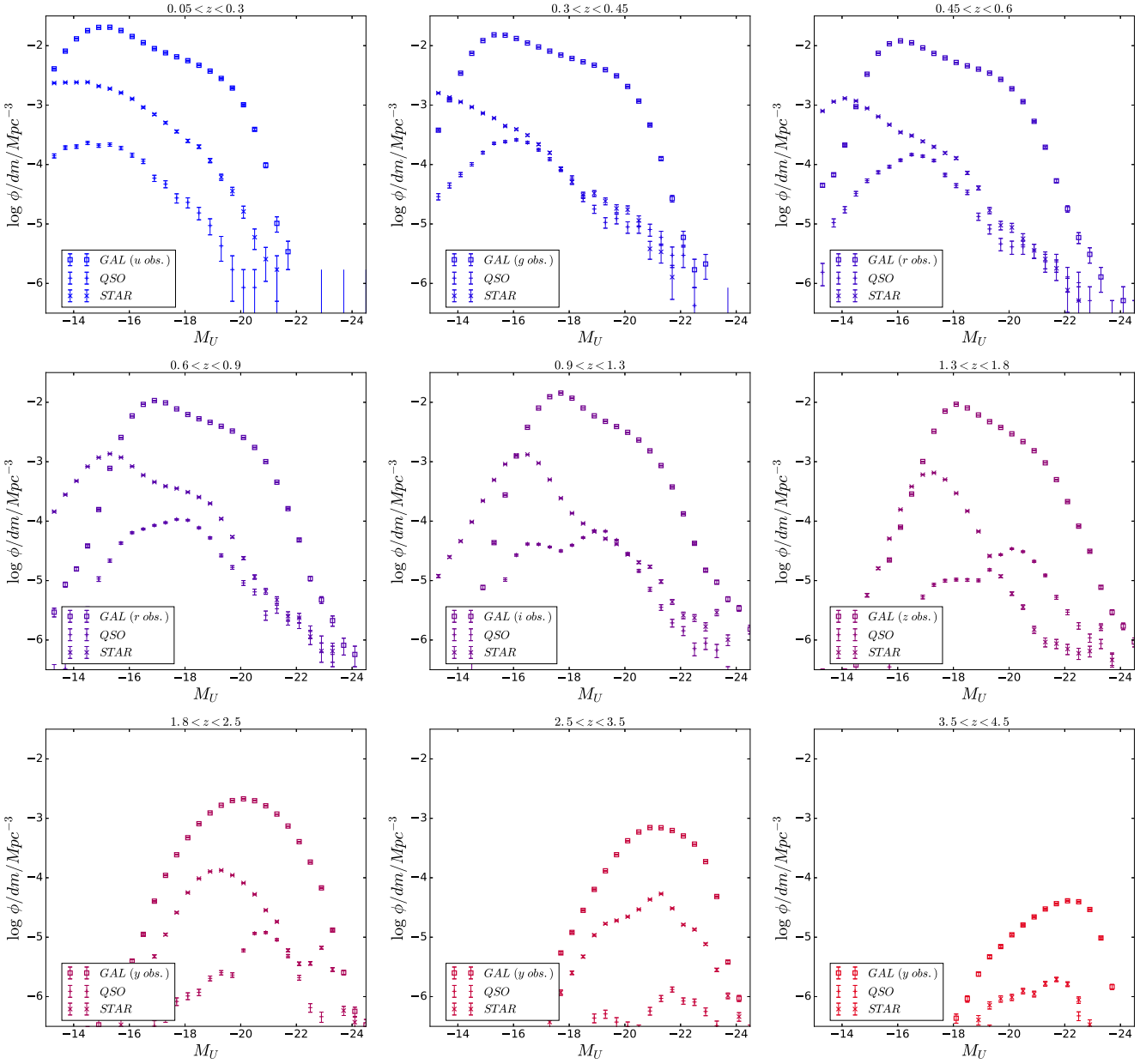

Figure C3. *U*-band LF of the different types of sources identified in our analysis: galaxies (GAL), quasars (QSO), and stars. The very bright end is mostly populated by stars and QSOs, which confirms that the deviation of the bright end of galaxy *U*-band LF from a pure Schechter form is likely to be due to contamination from stars and QSOs.

This paper has been typeset from a TEX/LATEX file prepared by the author.